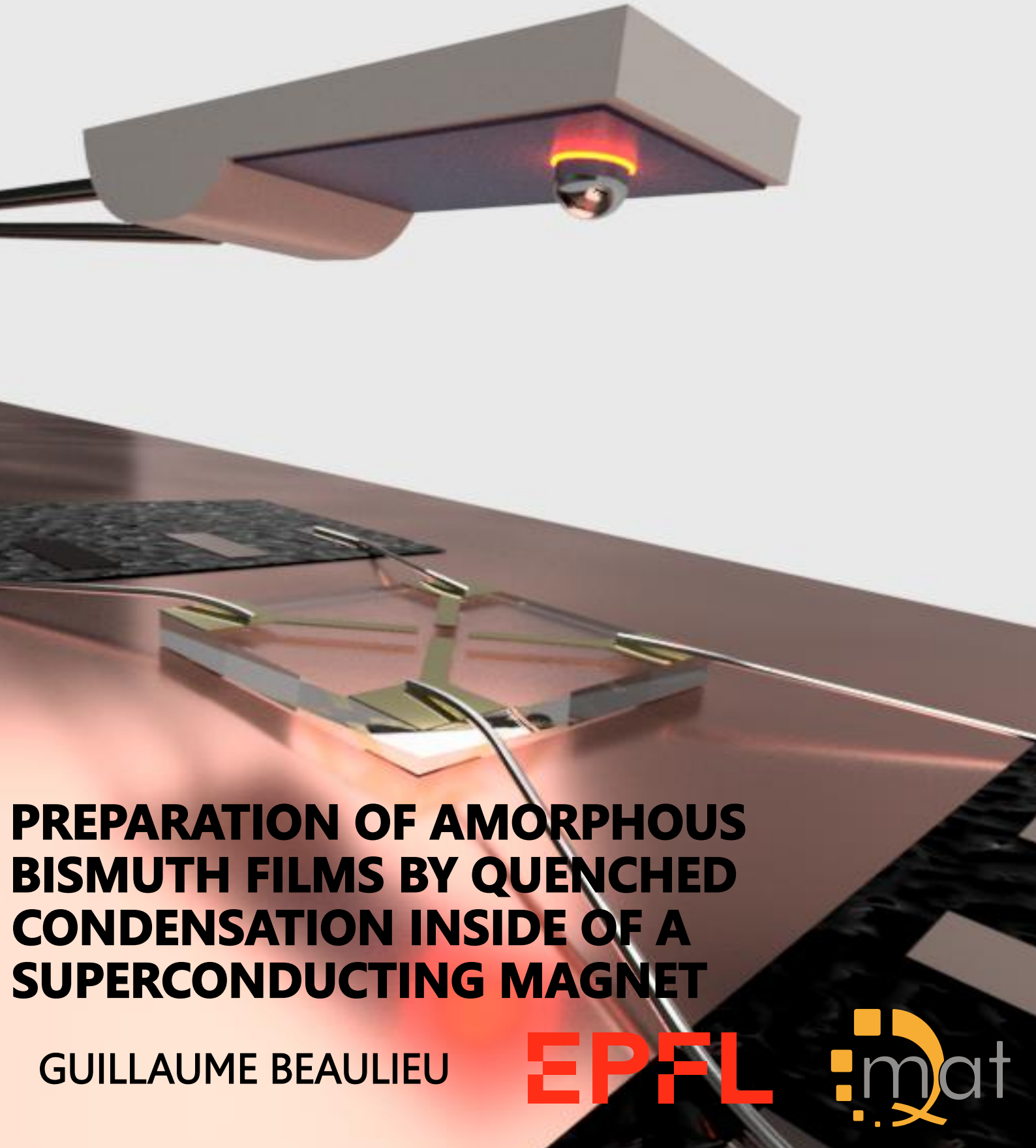# MASTER'S
THESIS

PREPARATION OF AMORPHOUS BISMUTH FILMS BY QUENCHED CONDENSATION INSIDE OF A SUPERCONDUCTING MAGNET

GUILLAUME BEAULIEU

EPFL :mat

Acknowledgements

First and foremost, I would like to thank Prof. Philip Moll not only for supervising this master's thesis, but also for welcoming me in his lab to be a part of many exciting projects throughout my master's degree at EPFL. Each project has revealed to be an outstanding learning opportunity that gave me a unique new insight on physics and research. This thesis has proven to be no exception. His patience, willingness to share his knowledge and expertise were deeply appreciated.

I would also like thank Dr. Kent Shirer and Dr. Carsten Putzke for their advice, explanations, and in general for all the time they took to support this work. I believe I will forever be in awe of their love of science, knowledge and technical skills.

Many thanks to the entire QMAT research group members who have each, at some point or another, helped me in my experiments.

I would also like to thank my friends for making this master's degree an incredible experience, and especially my roommates for being a true family in Switzerland.

A very special thanks to Anna for her support and for spending countless hours listening to me blab about amorphous bismuth; a subject which, I am sure, she is now passionate about.

Lastly, I could never thank my parents enough for their never-ending love and support.

Table of Content

Preparation of Amorphous Bismuth Films by Quenched Condensation Inside a Superconducting Magnet

Guillaume Beaulieu[1] supervised by Kent Shirer[1], Carsten Putzke[2], and Philip Moll[1,2]

[1] School of Engineering, École Polytechnique Fédérale de Lausanne, CH-1015 Lausanne, Switzerland
[2] Max Planck Institute for the Structure and Dynamics of Matter, 22761 Hamburg, Germany

Topological phases in crystalline materials have drawn intense research interest due to their fundamentally unique properties and potential for applications ranging from quantum computation to spintronics. Recently, scientists have extended the theoretical study of topology to a new class of materials: amorphous solids. Despite the growing interest in this new field, there remains a gaping need for new experimental tools to identify topological states in amorphous matter. Particularly challenging is the formation and study of amorphous metal films since they transform irreversibly to the crystalline state at very low temperature ($\sim$ 25 K). In the past, cryoevaporators were built to form metal films with extreme structural disorder by condensation onto substrates cooled to He-temperature. To avoid crystallization, these cryogenic systems had to be extremely large and include multiple cooling stages, shutters and heat shields to limit the heat flow to the substrate during the evaporation process (Fig. 1(A)). Although very successful in forming amorphous films, these cryoevaporators did not allow the application of the large magnetic fields needed to adequately probe topological properties. In this thesis, we solve this problem by building a compact evaporator that allows the formation of amorphous metal films directly inside of a superconducting magnet (Fig. 1(B)). Our system uses a simple off-the-shelf platinum-chip temperature sensor as a heating source to evaporate metals onto a sapphire substrate at He-temperature. The designed probe was used to form Bi films and measure the temperature dependence of their electrical resistance. The deposited films displayed a superconductive and crystallization transition, clearly indicating that we have successfully formed amorphous Bi. To showcase how the developed method can successfully probe amorphous metals in high fields, the film resistance was measured as a function of magnetic field up to 14 T. Reducing the cost into the one franc level and miniaturizing the size to cm^3, this work democratizes the study of amorphous Bi and expedites related studies into its topological nature.

1. Introduction

Topological materials have attracted intense research interest in recent years, as they exhibit fundamentally unique properties. Most of these properties arise from the so called bulk-boundary correspondence, which connects the topological structure of the bulk to surface states. A striking example of this principle occurs in topological insulators where metallic surface boundaries appear in spite of the bulk insulating state. These gapless boundary modes depend on the global structure of the material which makes them resilient to defects, impurities and other material imperfections. Due to their high robustness and special properties, these states hold great potential for applications ranging from quantum computing to spintronics (Chiu et al. 2016; Hasan

& Kane 2010).

Crystalline symmetries play a key role in our understanding and classification of the topological phases of matter. Nevertheless, the presence of translational symmetries is not an explicit requirement for the existence of topological states. In contrast to crystalline solids, the topological properties of systems subject to extreme structural disorder, such as amorphous metals, have been completely overlooked until recent years. The interface of topology and amorphous matter therefore remains an unexplored field which is not only of tremendous fundamental interest, but also holds great potential for technological developments. This new and exciting field of research motivates the search for new experimental tools allowing the study of the topological properties of amorphous metals (Grushin 2020).
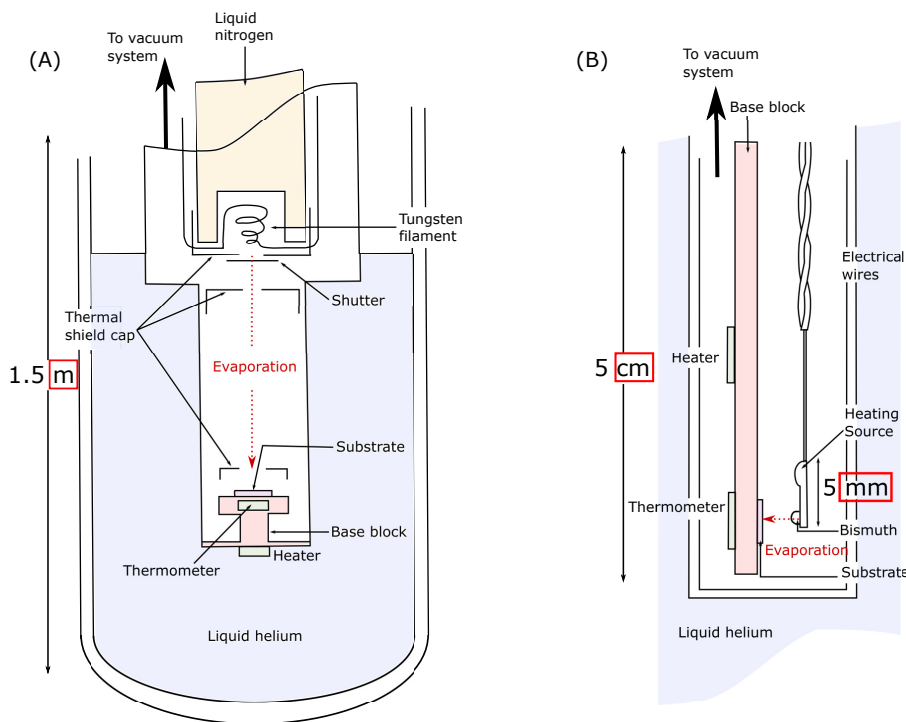
Fig. 1. **(A)** Schematic of a typical cryoevaporator used to form amorphous metals. The figure has been adapted from Hamada et al. (1981). **(B)** Schematic of the compact cryoevaporator developed in this work.

Amorphous metals are formed by quenched condensation, a process in which metal vapor is deposited on a substrate at cryogenic temperature. Atoms expelled from an evaporation source randomly strike a cold substrate and as a result are instantly "frozen" into a disordered configuration. The formed films are metastable and transform irreversibly to the crystalline state at temperatures on the order of ~ 25 K. Consequently, to avoid crystallization, the films must be formed under stringent conditions. In the past, this has been achieved by evaporating a metal from a hot tungsten filament onto a cold substrate inside of a cryostat under high vacuum. To limit the temperature rise and avoid crystallization during the deposition, the tungsten filament was generally positioned far from the substrate with multiple cooling stages, mechanical shutters and heat shields in between (Fig. 1(A)). This resulted in a large and complex cryogenic evaporation system that is not suitable for the study of topology. To adequately probe topological phases of matter, Landau quantization, obtained by applying a

strong magnetic field, is necessary. Consequently, to avoid crystallization and to have access to high magnetic fields, the amorphous films must be formed directly at the core of a superconducting magnet whose sample space is too narrow to accommodate such bulky evaporation systems. The goal of this thesis is to address this problem by developing the first compact cryoevaporator that fits inside a superconducting magnet. To test the designed system, we specifically aim to form amorphous bismuth films. Bismuth was chosen as the subject of study because it exhibits radically different properties in the amorphous state. As such, it is easy to identify if a disordered film has been successfully formed. In very practical terms, our goal can therefore be summarized as follows: heating Bi to its boiling point (~ 1000 K under high vacuum) inside a sample chamber measuring 2.5 cm in diameter and 10 cm in height with the substrate never exceeding the crystallization temperature of ~ 25 K.

This formidable technical challenge will be addressed in this thesis as follows. We will first introduce in section 2 how structural disorder influences the electronic and superconductive properties of Bi. In section 3, we will then present the experimental system designed to form amorphous Bi films. The results of the characterization of the deposited films will finally be presented and discussed in section 4.

2. Bismuth: Structural, Electronic and Superconductive Properties

Amorphous Bi is a prime candidate for the development of our evaporator because it displays properties radically different from those of its crystalline state. In particular, it has been found experimentally that the transition to the amorphous state results in a higher carrier density, a lower resistivity and a drastic change in the superconducting properties (Buckel & Hilsch 1954; Buckel 1959). These differences between the crystalline and amorphous states are of great importance because they will allow us later to assess whether we have succeeded in forming an amorphous film. Given their relevance for our work, we aim in this section to understand why these properties of Bi change when structural disorder is introduced. To answer this question, we will explore the characteristics of crystalline and amorphous Bi with the help of density functional theory (DFT) calculations. Unless specified otherwise, all calculations were performed with the Quantum Espresso (QE) software package developed by Giannozzi et al. (2009).

2.1. Crystalline Bismuth : Structural and Electronic Properties

To begin our study of Bi, we first introduce the atomic structure of the crystalline state and explain its strong influence on the electronic properties of Bi. Most elemental metals crystallize into a simple cubic (FCC or BCC) or hexagonal closed-packed structure (HCP) to minimize interatomic forces. The Bi crystal structure is a peculiar case. It is almost perfectly cubic with every second atom displaced by a short distance along the diagonal axis with the angle between the axes differing slightly from 90° (Fig. 2(A)) (Peierls 1991). As a result of this deformation, the primitive cell of Bi is not cubic, but rhombohedral (space group R$\bar{3}$m, A7 arsenic structure) with two atoms per unit cell (Fig. 2(C)). The cell and atomic positions are fully determined by three parameters: the rhombohedral cell length (a_{rho}), the rhombohedral angle (α_{rho}) and the internal parameter (u).

The internal parameter defines the position of the atoms along the trigonal axis (u, u, u) and $(-u, -u, -u)$ in units of a_{rho}. The lattice parameters used in this work are a_{rho} = 4.798 Å, α_{rho} = 57.423° and u = 0.2672 (Jain et al. 2013). Alternatively, the A7 structure can be represented by an hexagonal conventional unit cell containing 6 atoms (Hofmann 2006). The hexagonal representation shown in Fig. 2(B) highlights how a Bi crystal is formed by stacking bilayers of atoms perpendicularly to the rhombohedral [111] direction.
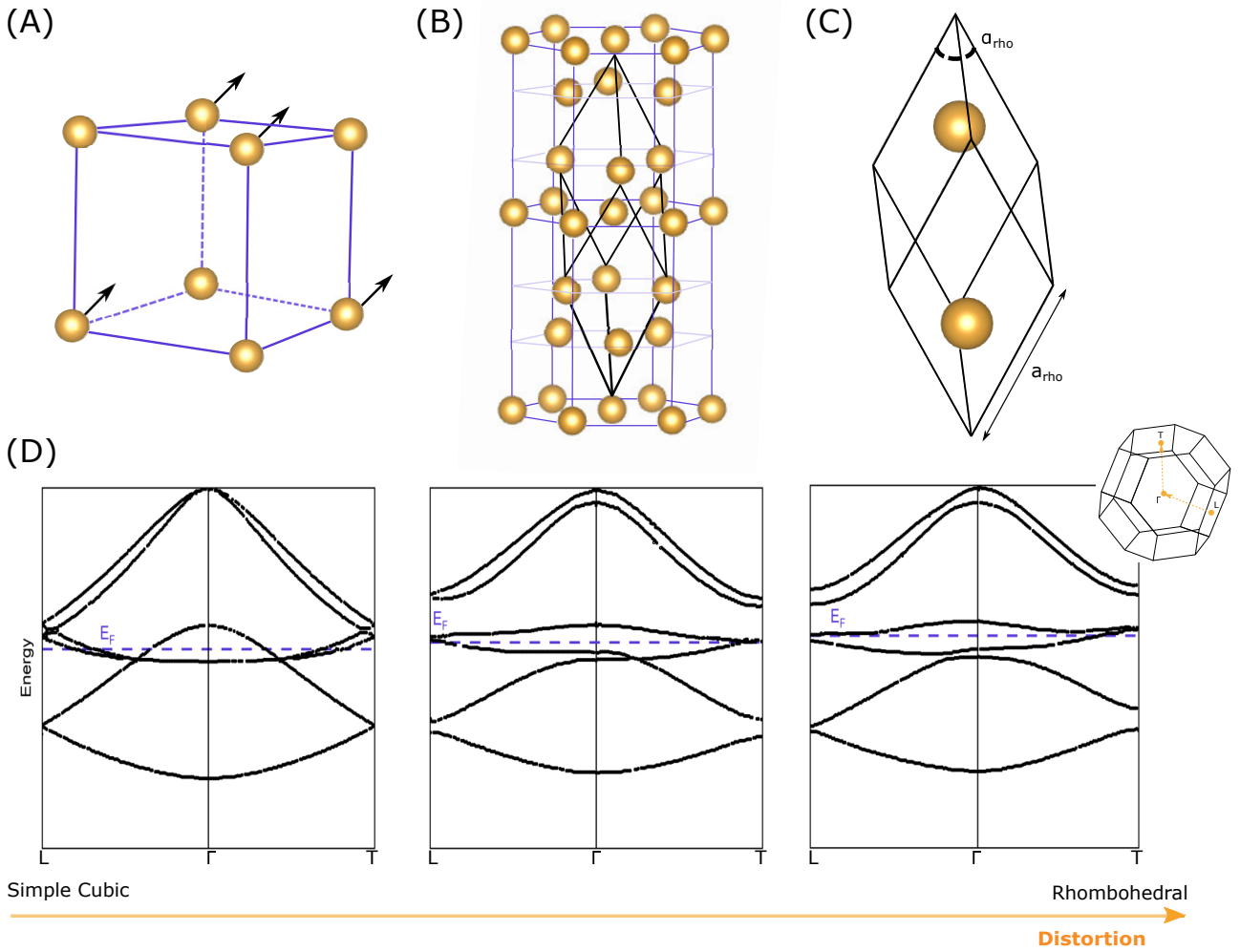
Fig. 2. (**A**) Deformation of the simple cubic structure into the R$\bar{3}$m structure. The figure is adapted from Peierls (1991). (**B**) Hexagonal conventional unit cell (purple) of bulk Bi showing its layered structure. The rhombohedral primitive unit cell is identified in black and also shown in (**C**) for clarity. (**D**) Schematic illustration of the effect of the Bi lattice distortion on the band structure. For a cubic configuration (left panel), the p-band is half-filled (metal). By dimerization, an energy gap which lowers the total electronic energy of the system opens (middle panel). In the actual rhombohedral structure (right panel), the distortion leads to a small electron and hole pocket at L and T respectively (semimetal). The figure has been adapted from the calculations of Shick et al. (1999)

.

The unusual crystal structure of Bi is deeply linked to its electronic structure and unconventional properties. Bismuth is a pentavalent semimetal with electronic configuration: [Xe] $4f^{14}5d^{10}6s^26p^3$. If Bi were in a perfect cubic configuration, it would be metallic as a result of the odd number of electrons ($6s^26p^3$) per unit cell. This is illustrated by the DFT calculated band structure of Bi in a cubic arrangement shown in the left panel of Fig.

2(D)) (Shick et al. 1999). However, as discussed above, the deviation of the system from the cubic structure lowers the system symmetry and creates two atomic sites per unit cell. In the resulting rhombohedral state, Bi has an even number of valence electrons per unit cell (10 electrons). Consequently, an insulator could be expected. In reality, the deviation from the cubic structure is analog to a 1D-Peirls distortion and results in a reduction of the Brillouin zone. Due to the reconstruction of the Brillouin zone, part of the Fermi surface is gapped out leaving only small pockets responsible for the semimetallic behavior of the material. In Bi, since the edge of the Fermi distribution nearly coincides with the gap opening, this distortion is favorable because all of the occupied states are displaced downward in energy while the energy of all of the empty states is raised. The consequence is a net energy reduction that more than compensates for the elastic energy cost of the deformation (Peierls 1955, 1991). The metallic to semimetallic transition due to the distortion is illustrated by the schematic band structures shown in Fig. 2(D). This simple picture can be further developed by DFT electronic structure calculations.

The DFT calculations were performed with a plane wave basis and charge density expanded up to a cutoff charge density and kinetic energy of 55 Ry and 450 Ry respectively. A full relativistic pseudopontential from the QE PSlibrary (Dal Corso 2014) was used to include the effects of spin-orbit coupling (SOC). The self-consistent calculation was carried out with an 18x18x18 Monkhorst-Pack grid of the primitive cell in the reciprocal space. These DFT parameters were chosen following convergence tests on the ground state energy. For metals, computing properties by performing integrals in the reciprocal space can be complicated because the integrand changes discontinuously at the Fermi surface. To overcome this complication, the discontinuity of the function to be integrate is generally "smeared out". Here, the Marzari-Vanderbilt cold smearing scheme was used with the smearing parameter set to 0.01 Ry (Marzari et al. 1999). The computed electronic bands (including SOC) along certain high symmetry lines of the first Brillouin zone are shown in Fig. 3(A). The band structure can be understood as two filled 6s bands (around -10 eV and not shown in the figure) well separated from the three filled 6p valence bands. The 5d electrons lie below -20 eV and are not shown in the figure. In the vicinity of the T point, the highest valence band crosses the Fermi level creating a hole pocket. Similarly, at the L point, an electron pocket is generated by the crossing of the lowest conduction band (Hofmann 2006; Liu & Allen 1995). The small pockets of carriers imply a small Fermi surface (Fig. 3(C)) and a very low electronic density of states (eDOS) at the Fermi energy as displayed in Fig. 3(B). The computed eDOS is shown to be in good agreement with the previous theoretical works of Timrov (2013) and Gonze et al. (1988). The large decrease in the eDOS around the Fermi energy explains why the carrier density in Bi (2×10^{17} cm^{-3}) is reduced from typical metal densities by a factor of 10^5 (Issi 1979; Ashcroft et al. 1976).
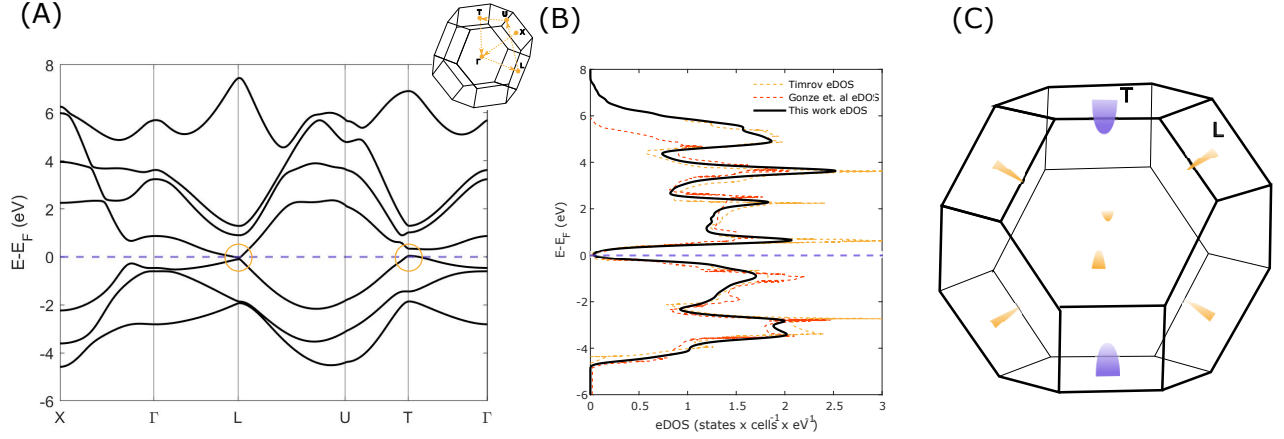
Fig. 3. (**A**) Calculated DFT band structure with SOC. The hole and electron pockets at the *T* and *L* points are highlighted by yellow circles. The high symmetry points are labelled on the Brillouin zone shown in the inset. (**B**) eDOS of bulk Bi and comparison with other theoretical works by Timrov (2013) and Gonze et al. (1988). (**C**) Brillouin zone and schematic sketch of the Bi Fermi surface (not to scale). The hole pockets are drawn in purple and the electron pockets in yellow.

2.2. Amorphous Bismuth: Structural and Electronic Properties

In order to understand how the electronic structure of crystalline Bi changes with the loss of periodicity and leads to the experimental observations mentioned above, we simulate here an amorphous Bi cell and compute its eDOS. To adequately simulate the formation of an amorphous structure, it is useful to begin by reviewing some fundamental principles of crystallization. Crystallization occurs by a nucleation and growth process. For a small crystalline region embedded in an amorphous matrix (e.g. a melt) cooled below the melting point, there is a trade-off between lowering the free energy of the system by favoring the growth of the equilibrium crystalline phase and increasing the interfacial energy (crystal/amorphous). As a result, there exists a critical size r_c of the crystal grain above which the energy of the system decreases with the grain growth. Consequently, the nucleation and growth of the crystalline phase can be prevented by hindering the thermodynamic fluctuations that lead to random aggregation of atoms of size larger than r_c (Clemens 1983; Ohring 2001; Christian 2002). In practice, this is generally achieved by reducing the mobility of the atoms using a wide range of techniques: (i) evaporation or sputtering onto substrates at low temperature; (ii) particle irradiation onto crystals at low temperature; (iii) ion-mixing or implantation (iv) liquid quenching, etc (Foner & Schwartz 2012). For a simple single phase crystalline structure like Bi, the atomic motions required for crystallization are generally not extensive or complex. Consequently, the system can form stable crystalline nuclei at very low temperature, i.e. 25 K in Bi. For this reason, amorphous Bi is generally formed by quenched condensation (Buckel & Hilsch 1954; Reale 1978; Minnigerode & Rothenberg 1968; Chen et al. 1967; Hamada et al. 1981). In quenched condensation, Bi is evaporated under high vacuum. The atoms expelled from the source randomly hit a substrate at He-temperature. If the substrate temperature remains low during evaporation, the atoms almost instantly lose their kinetic energy striking the cold surface. By drastically reducing atomic motion, the nucleation and growth of the crystal is inhibited (Bergmann 1976). It is clear that the generated amorphous phase is metastable and will transform irreversibly to the crystalline state when the temperature increases above ~ 25 K and the atomic

motion becomes large enough for the stable nuclei to grow.

In this work, we generated an amorphous Bi cell by simulating the quenched condensation process by ab initio molecular dynamics. For this, we began with a crystalline supercell containing 128 atoms. The supercell corresponds to 4x4x4 times the primitive Bi cell. To introduce disorder, the cell was melted by increasing the system temperature to 800 K in 100 steps of 27 fs. Once the cell was melted, the quenching was simulated by a structural relaxation process. The initial crystalline supercell and the generated amorphous structure are shown in Fig. 4(A). The structure of the amorphous Bi cell cannot be described by a set of basis vectors as
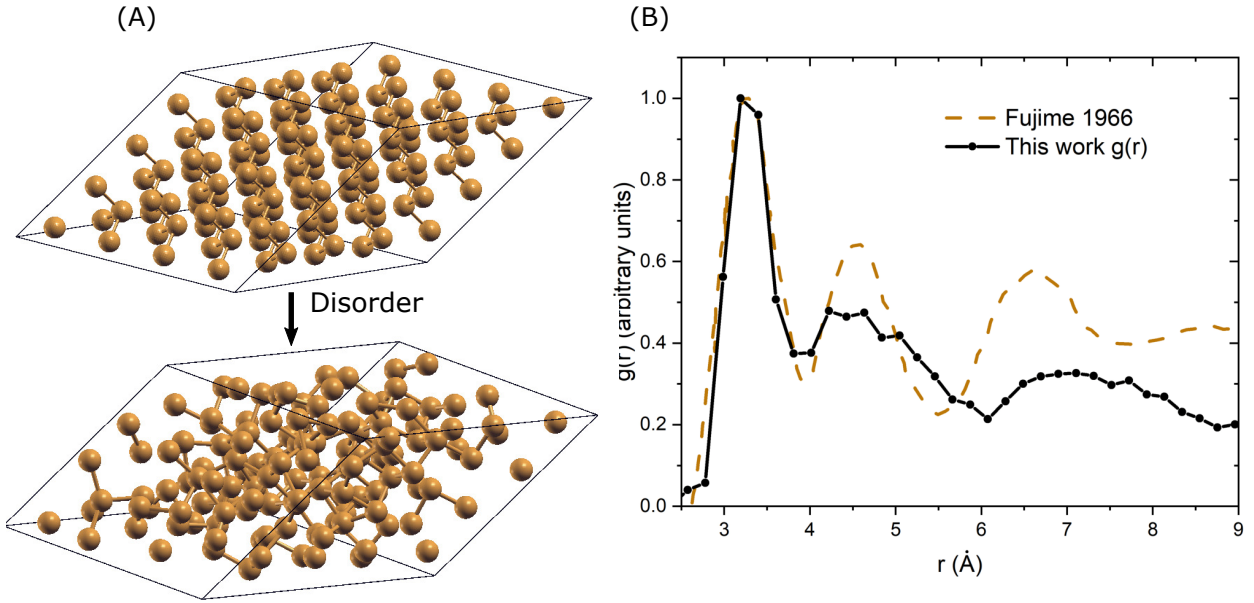

Fig. 4. (**A**) Initial crystalline supercell and its corresponding amorphous Bi cell resulting from the ab initio molecular dynamics calculations. (**B**) Normalized radial distribution function of the computer-generated amorphous supercell compared to the experimental curve measured by Fujime (1966).

in the crystalline state because of the loss of translational symmetry. Instead, the system is described by the averaged relative position of the atoms using the radial distribution function $g(r)$ (RDF). The function $g(r)$ is constructed by choosing a reference atom and counting the number of atoms in a shell of thickness dr at a radius r. This number is then normalized with respect to an ideal gas $\rho 4\pi r^2 dr$ to obtain the RDF. By electron diffraction, Fujime (1966) measured the RDF of amorphous Bi formed by quenched condensation. The comparison between the experimental curve and the computationally generated amorphous Bi structure is shown in Fig. 4(B). The RDF of the amorphous cell was calculated with the ISAACS software (Le Roux & Petkov 2010). For comparison with the experimental curve, the computed RDF was smoothed so that the height of the maximum peak matches the experimental height. The simulated RDF quickly diverges from the experimental result due to the limited size of the system. It can be seen, from both the experimental and theoretical curves, that the RDF is characterized by a large peak (first neighbors) followed by damped oscillations (second and third neighbors). This indicates that a considerable level of short range order remains

in the amorphous state due to the hard ion cores.

The eDOS of the generated amorphous cell was calculated using the same cutoff parameters as in the crystalline case and a 4x4x4 Monkhorst-Pack grid of the supercell in the reciprocal space. The computed eDOS is shown in Fig. 5. The result is in good agreement with the work of Mata-Pinzón et al. (2016) who computed the eDOS for an amorphous Bi supercell of 216 atoms. For comparison purposes, the result of Mata-Pinzón et al. (2016) was divided by a constant so that its curve has the same maximum value as ours. From our calculations, we see that the eDOS at the Fermi level in the amorphous state is roughly $\sim 10^4$ times that of the crystalline state. As discussed in subsection 2.1, crystalline Bi has a semimetallic electronic structure as a result of the Fermi surface-Brillouin zone interaction. The concept of the Brillouin zone is derived from the Fourier transform of the periodic lattice in real space. In the amorphous structure, the loss of long range order therefore implies the disappearance of the Brillouin zone. In other words, due to the loss of periodicity, the electrons no longer experience Bragg reflections. In Bi, this implies that the gap opening responsible for the semimetallic behavior of the material also disappears. This results in the observed semimetallic to metallic transition manifested by a substantial increase in the eDOS at the Fermi level. As expected, the disappearance of the Brillouin zone boundaries also eliminates the details present in the eDOS of crystalline Bi (Fig. 3(A)). Hence, the amorphous eDOS is essentially a smoother version of the crystalline eDOS (Chen 1980).
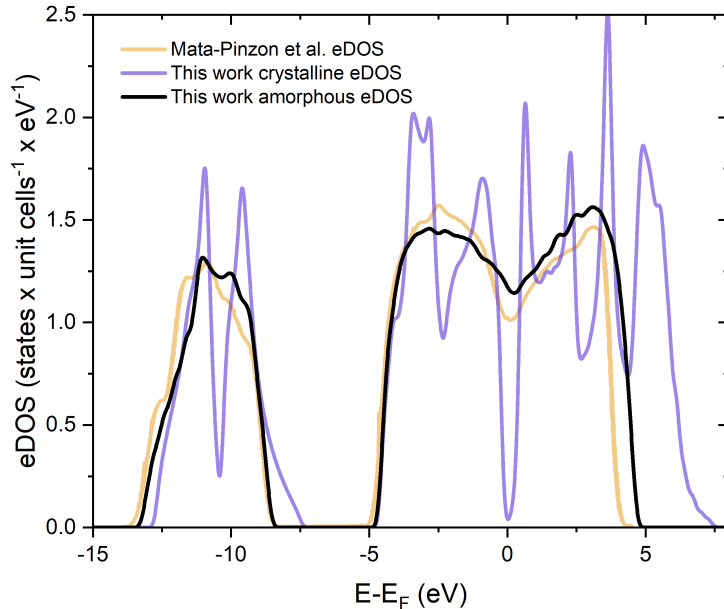
Fig. 5. eDOS of the generated amorphous Bi supercell and comparison with the calculation of Mata-Pinzón et al. (2016) and the crystalline eDOS.

Based on the calculations shown above, we now seek to understand how the change in the electronic structure explains the high conductivity and electronic density observed in amorphous Bi. For this, it would be ideal to have a theory of amorphous metals. However, the breakdown of the concept of crystal momentum and Bloch waves in disordered structures makes it particularly challenging to derive such theory. The Ziman theory

(Ziman 1961), developed for liquid metals, is one of the most successful descriptions we have for explaining the properties of non-periodic metals. In the Ziman theory, the difficulties associated with the loss of the crystal momentum are essentially ignored. The electrons are simply treated as plane waves representing free electrons (Bergmann 1976). The electron transport is then described by the Boltzmann theory with the particularity that each atom can act as a scattering center due to the disorder. The effect of the ions on the electrons is represented by a pseudopotential with the loss of periodicity taken into account by the structure factor derived from the RDF (Mizutani 1983; Dugdale 2016). From electron diffraction experiments on amorphous Bi performed by Fujime (1966) and on liquid Bi by Waseda & Suzuki (1972), we know that the structure of the amorphous metal has features similar to that of the liquid metal. Consequently, given the success of the free electron model in describing the properties of liquid metals, we apply a similar treatment to amorphous Bi. In the free electron model, the electron density n and the conductivity σ can be calculated as a function of the eDOS at the fermi level $g(E_F)$ using the following equations

$$n = \frac{1}{3\pi^2} \left(\frac{g(E_F)\pi^2\hbar^2}{m} \right)^3 \tag{1}$$

$$\sigma = e^2 D g(E_F) \tag{2}$$

where m is the free electron mass and D is the diffusion coefficient. From Eqs. 1 and 2, it becomes clear why the substantial increase of $g(E_F)$ in the amorphous state is accompanied by an increase in carrier density and conductivity. It is however important to note that for the conductivity, the increase in $g(E_F)$ is partly compensated by a decrease in the diffusion coefficient due to the higher degree of scattering in the disordered film. The change in σ and n will later be particularly useful to monitor the transition from the amorphous to the crystalline state.

The free electron model can be used to make further qualitative predictions about the expected properties of amorphous Bi films. Assuming the density in the amorphous structure is the same as in the crystalline structure (9.8 g/cm^3 (Lide 2004)) and taking 5 valence electrons per atom, we calculate an electron density of $n = 1,4 \times 10^{23}$ cm^{-3}. Given the electronic density, we calculate several important parameters of the free electron model (Ashcroft et al. 1976):

$$v_F = \frac{\hbar}{m}(3\pi^2 n)^{1/3} \tag{3}$$

$$E_F = \frac{m v_F^2}{2} \tag{4}$$

$$l_e = \frac{m v_F}{n e^2 \rho} \tag{5}$$

The calculated Fermi velocity is $v_F = 1.9 \times 10^8$ cm/s and the Fermi energy is $E_F = 9.8$ eV. Using the resistivity value of $\rho = 100\,\mu\Omega$cm experimentally measured by (Shier & Ginsberg 1966), the calculated mean free path is $l_e = 4.60$ Å. These theoretical predictions will later be verified experimentally and discussed.

2.3. Characteristics of Superconductivity in Amorphous Bismuth

The differences between the electronic structure of amorphous and crystalline Bi, introduced in the previous subsections, result in radically different superconductive properties in the two states. These differences will later be extremely useful in determining whether our Bi film is in an amorphous or crystalline state. For this reason, we point out here some of the expected changes in the superconducting properties and explain why they arise.

Superconductivity has been observed in pure Bi crystals below 0.53 mK (Prakash et al. 2017). In contrast, amorphous Bi was found to superconduct below 6.1 K in the amorphous state (Buckel & Hilsch 1954; Hamada et al. 1981). This impressive increase in the critical temperature T_c can be qualitatively understood in terms of Peirls distortion. As discussed above, the crystallization of Bi in a rhombohedral primitive cell introduces a gap opening in the electronic structure. The effect of this gap opening on the superconductivity of crystalline Bi is twofold. First, it reduces the Fermi surface and density of states at the Fermi level. Secondly, the Bloch electrons near the Fermi surface screen effectively the lattice potential since they are concentrated in potential valleys. The loss of long-range order eliminates these two effects. This leads to a higher density of states and a more efficient electron-phonon interaction in amorphous Bi, both of which favor the formation of Cooper pairs and a larger value of T_c. The measurement of a high T_c is therefore a key indicator of a disordered Bi film.

There are other important parameters of superconductivity which give a great indication of the loss of periodicity. Most of these parameters can be defined in the framework of the phenomenological Ginzburg-Landau (GL) theory. In particular, the GL theory defines two characteristic lengths central to the study of superconductivity. The first characteristic length λ_L is called the London penetration depth and is given by

$$\lambda_L(0) = \sqrt{\frac{m}{\mu_0 n_s e^2}} \tag{6}$$

where m and e are respectively the electron mass and charge, μ_0 is the vacuum permeability and n_s is the density of superconducting carriers. The London penetration depth corresponds to the length-scale over which a magnetic field is screened out to zero inside a superconductor. The second characteristic length, called the coherence length ξ, defines the distance over which the superconducting wave function varies. This coherence length is given by

$$\xi(T) = \sqrt{\frac{\hbar^2}{2m_s\,|a(T)|}} \tag{7}$$

where $a(T)$ is a coefficient introduced in the GL theory. The ratio of the two characteristic lengths $\kappa = \lambda_L(T)/\xi(T)$ is called the Ginzburg-Landau parameter. Type I or type II superconductors are respectively distinguished according to whether $\kappa < 1/\sqrt{2}$ or $\kappa > 1/\sqrt{2}$.

The characteristic lengths defined in Eqs. 6 and 7 are only valid in what is called the "clean limit" of the GL theory. In this limit, the material is assumed to be highly ordered with very few defects and impurities. An amorphous film does not fall in this limit since the high level of structural disorder leads to additional electron scattering sites. This results in an electron mean free path l_e much smaller than both the coherence length ($l_e \ll \xi(T)$) and the London penetration depth ($l_e \ll \lambda_L(T)$). Under these conditions, the specimen is said to be in the "dirty limit" of the GL theory. Since $l_e \ll \xi(T)$, the electrons involved in the Cooper pairing undergo multiple scattering events during their lifetime. This reduces the size of the Cooper pairs according to (Saint-James et al. 1969)

$$\xi_d(T) = 0.85 \, (\xi_0(0)l_e)^{1/2} \left(\frac{T_c}{T_c - T} \right)^{1/2} \tag{8}$$

with $\xi_0(0)$, the BCS coherence length of a "clean" material, given by

$$\xi_0(0) = \frac{\hbar v_F}{\pi \Delta(0)} \tag{9}$$

where v_F is the electron band velocity at the Fermi surface and $\Delta(0)$ is the gap size at 0 K. On the other hand, the increase of the electron scattering decreases the effectiveness of the field screening. The London penetration depth is thus decreased to (Saint-James et al. 1969)

$$\lambda_d(T) = 0.615 \lambda_L(0) \left(\frac{\xi_0(0)}{l_e} \right)^{1/2} \left(\frac{T_c}{T_c - T} \right)^{1/2} \tag{10}$$

Due to their dependence on the degree of scattering, $\lambda_d(T)$ and $\xi_d(T)$ are good parameters to characterize the level of disorder in a film. From the above discussion, we expect in amorphous Bi a large λ_d, a small ξ_d, and thus a large ratio for $\kappa = \lambda_d/\xi_d$ indicating a type II superconductor. Lastly, since the upper critical field H_{c2} of a type II superconductor is related to the critical field H_c by the following equation

$$H_{c2} = \sqrt{2}\kappa H_c \tag{11}$$

we also anticipate that the large value of κ will lead to a high H_{c2}.

3. System Design & Methods

Following the theoretical study of the properties of Bi, we now turn to the experimental methods developed during this work to form amorphous films. In the past, disordered Bi films were formed by evaporating Bi pellets from hot tungsten filaments onto cold substrates under high vacuum. To ensure that the substrates always remained below the crystallization temperature of 25 K during deposition, the evaporation systems

were built in large cryostats comprising several cooling stages, shutters and heat shields. These bulky and complex cryoevaporators are not suitable for the study of topology since they cannot be transferred inside the sample chamber of a superconducting magnet system whose typical dimensions are 2.5 cm in diameter and 10 cm in height. Indeed, to adequately probe potential topological phases in amorphous Bi, uniform magnetic fields must be applied to quantize the electrons' circular orbits into Landau levels. Hence, the goal of this thesis: designing and building the first compact evaporation system allowing the formation of amorphous Bi inside a superconducting magnet. Important challenges that we face in achieving this goal are the low crystallization temperature of Bi and the restricted space inside the magnet. Additionally, since the sample chamber of the magnet sits ~ 1 m below the opening of the dewar containing the magnet, the evaporation system must be mounted on a long probe. In this section, we present how we tackled these difficulties by revisiting and downsizing the standard thermal evaporation approach. The fundamentals of thermal evaporation are first introduced, followed by the characterization of our evaporation source and the design of our probe.

3.1. Fundamentals of Thermal Evaporation

A thermal evaporation process involves a few key parameters. In this short introduction to the fundamentals of thermal evaporation, we aim to understand the interplay between these parameters so that we can choose a suitable heating source and appropriate evaporation conditions for our system. In a thermal evaporation process, an evaporation source is used to heat a material until a desired evaporation rate is reached. The attained rate is directly dependent on the material vapor pressure P_e. In thermodynamic equilibrium, the vapor pressure of a material corresponds to the pressure that develops over the material in a closed chamber at fixed temperature. The vapor pressure increases with temperature, but the exact dependence of P_e on T is complex and requires careful evaluation of thermodynamic data for each material and pressure range (Ohring 2001; Siddall 1971).

For a system out of thermodynamic equilibrium, the vapor pressure defines the flux of atoms that are expelled from the condensed phase at a given temperature. This flux is however partly compensated for by the atoms in the atmosphere at ambient hydrostatic pressure P_h that impinge on the evaporating surface. The net evaporation flux Φ_e is the difference between these two contributions. From the kinetic theory of gas, Φ_e, in number of atoms per unit area per unit of time, can be calculated according to the Hertz-Knudsen equation

$$\Phi_e = \frac{\alpha_e(P_e - P_h)}{(2\pi mRT)^{1/2}} \tag{12}$$

where R is the ideal gas constant, m is the atom mass and $0 \leq \alpha_e \leq 1$ is the probability that a vapor molecule sticks to the surface. The evaporated mass from a surface of area A_e is then simply given by the double integral
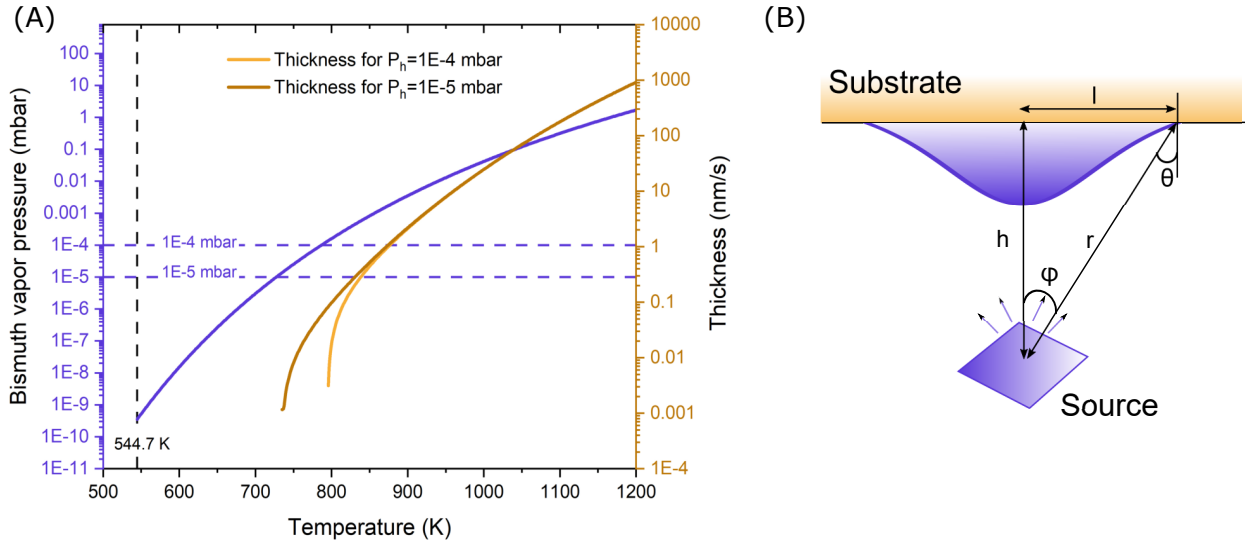
$$M_E = \int_0^t \int_{A_e} \frac{\Phi_e}{m} dA_e dt \tag{13}$$

Knowing M_E from the previous equation, the film thickness t and film uniformity may be calculated by simple geometric considerations. For a surface source, one finds a thickness

$$t = \frac{M_e \cos\theta \cos\phi}{\pi\rho r^2} = \frac{M_e h^2}{\pi\rho(h^2 + l^2)^2} \tag{14}$$

where ρ is the material density and the other geometric parameters are defined in Fig. 6 (B).

Fig. 6. (**A**) The vapor pressure of Bi as a function of the temperature is shown in purple. A vapor pressure of 1×10^{-4} mbar and 1×10^{-5} mbar are respectively achieved for temperature of 730 and 800K. The evaporated thickness per second at $l = 0$ (maximum) is shown in yellow. A deposition rate of ~ 5 nm/s is achieved for a source temperature around 900K. (**B**) Geometric parameters used in the calculation of the deposited thickness (Eq.14).

The vapor pressure of Bi as a function of temperature is shown by the purple curve in Fig. 6(A) (Lide 2004). From Eq. 12, it is clear that evaporation can occur only if the ambient hydrostatic pressure is lower than the vapor pressure. Since the systems used during this thesis reach typical vacuum level between 1×10^{-4} mbar and 1×10^{-5} mbar, Bi must be heated to a temperature of at least 730 K or 800 K in order to evaporate. This temperature range, well above the 545 K melting point (Lide 2004), illustrates how crucial it is to achieve a high vacuum level to minimize the amount of heat in the system. From the Bi vapor pressure, the maximum evaporated thickness t ($l = 0$) was calculated for a hydrostatic pressure of 1×10^{-4} mbar and 1×10^{-5} mbar using Eqs. 12, 13 and 14. The result is given by the yellow curves in Fig. 6(A). For the calculation, we used $\rho = 9.78$ g/cm^3 (Lide 2004), assumed $h = 1$ cm, $\alpha_e = 1$ and an evaporating surface area corresponding to a Bi sphere of 1 mg. It can be seen from this calculation that an appreciable deposition rate (~ 5 nm/s) is only achievable for a source temperature around 900 K.

Multiple important conclusions may be drawn from the above analysis. (i) To minimize the evaporation temperature and avoid any surface contamination of the deposited layer, a very high vacuum level is required.

(ii) To achieve a sufficiently high evaporation rate, the heating source must be able to withstand a temperature of 900 K or more. (iii) For such high temperatures, the exact pressure does not significantly influence the deposition rate. (iv) Lowering the source-substrate distance leads to a considerably higher deposition rate ($t \propto 1/h^2$), but impacts the film uniformity ($\mathrm{d}t/\mathrm{d}l \propto 1/h^4$).

3.2. Heating Source and Evaporation Procedure

The first step in depositing Bi by thermal evaporation was to identify a suitable heating source. Based on the previous discussion, we know that our evaporation source had to meet several requirements. The source had to have a negligible vapor pressure compared to Bi and be chemically inert. It also had to be able to withstand temperatures above 900 K, fit in the available space, and dissipate the minimum amount of heat required. As briefly mentioned in section 3, tungsten wire sources were extensively used to form amorphous Bi. Tungsten wire baskets operating at temperatures greater than 2000 K and having a diameter and height of less than 10 mm are commercially available. However, within the size constraints, even very thin tungsten wire sources have low resistance ($\sim 0.1\ \Omega$). Reaching a sufficiently high temperature to evaporate Bi would require current on the order of ~ 1 A. The meter long lead wires required to reach the magnet sample space would have a resistance of the same order of magnitude as the evaporation source. Consequently, passing such high current through these wires risks damaging them and heating the system by several kelvins. Furthermore, considering the limited space, a tungsten wire basket would be bulky and dissipate a lot of undesirable heat. For these reasons, we present and characterize in this section a new evaporation source better adapted to our task.

The chosen evaporation source was a thin-film micro-heater. This type of source, although never used in standard evaporation systems, offers many advantages for our specific purpose. Its large resistance and small physical size allows dissipating heat locally and preventing losses in the lead wires. To ensure the thin film heater functionality at high temperature, we opted for an off-the-shelf platinum-chip temperature sensor (PT100) model PCA 1.1505.1M from JUMO. The PT100 has a meandered platinum resistance deposited by sputtering over a $5 \times 1.5 \times 0.38$ mm sized ceramic, and patterned via a lithographic process. To insulate and protect the resistance against external influence, the platinum thin film is coated by a glass layer. Two 10 mm long and 200 μm diameter platinum-nickel wires are welded onto the contact surface to make electrical connections with the resistor. An exploded view of the sensor is shown in Fig. 7(A) (P10 2002). As a temperature sensor, the PT100 provides a fast response time and is rated for a relatively wide temperature range (203 K-823 K).

Since the PT100 is designed for thermometry purposes, it was important to first determine if it could also be used to evaporate Bi. For this, we designed a simple benchtop vacuum chamber. The vacuum chamber was on one side connected to a turbomolecular pump and on the other had a flange with a 10 pin electrical Fischer

connector (Fig. 7(C)). At the center, there was a copper cylinder designed to hold a suspended heater via two side screws. The suspension of the heater limited heat loss by conduction in the copper. A small slit was cut at the top of the cylinder to place a microscope glass slide above the evaporation source (Fig. 7(B)). A simple Plexiglas window was placed on top of the vacuum chamber to observe if Bi condensation appeared on the glass slide.
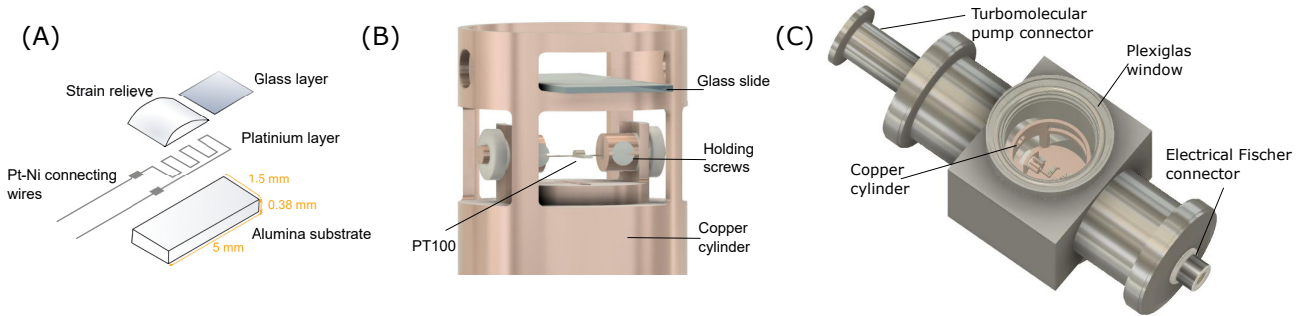

Fig. 7. (**A**) Exploded schematic of the PCA 1.1505.1M thermometer from JUMO. The figure is adapted from P10 (2002). (**B**) Schematic of the copper cylinder designed to hold the suspended PT100. The PT100 is suspended by the two screws labelled holding screws and evaporates onto the glass slide. (**C**) Schematic of the designed evaporation chamber. The chamber is pumped from the turbomolecular pump connector. Any element inside is connected via the electrical Fischer connector. From the Plexiglas window on top, the evaporation process can be observed.

To establish if we could successfully evaporate Bi, 0.5 mg of Bi 99.999 % from Sigma-Aldrich was positioned on the suspended PT100 and the chamber was pumped to 1×10^{-4} mbar. Using the Keithley 6221 current source, the current through the resistor was gradually increased while monitoring the applied voltage. Since the PT100 is made for thermometry purposes, the temperature of the heating element was directly deduced from the measured resistance using a general calibration curve :

$$R(T) = R_0(1 + A \cdot T + B \cdot T^2) \tag{15}$$

with $A = 3.90802 \times 10^{-3} \,^{\circ}C^{-1}$ and $B = -5.775 \times 10^{-7} \,^{\circ}C^{-2}$ (Nau 2002). The measured steady-state temperature as a function of current is presented in Fig. 8(A). Bismuth condensation on the glass plate became visible at temperatures above 893 K which is consistent with the calculations presented in section 3.1. Past 1150 K, the thin film resistor began to degrade and subsequent temperature measurements were not accurate. These results show that we can use the PT100 to evaporate Bi. However, reaching the threshold temperature for evaporation at current of 38 mA took $\sim$ 100 s. For the formation of amorphous Bi at low temperatures, heating the source for this long may considerably increase the sample space temperature and crystallize the deposited film. To reduce the heating time, the direct current was replaced by a short current pulse. To assess how quickly Bi can be evaporated, we measured the time required for the PT100 to reach the evaporation temperature as a function of the applied current under a vacuum of 1×10^{-4} mbar. The results are displayed in Fig. 8(B). For the Keithley maximum output current of 105 mA, evaporation occurred for a minimum pulse length of 1.5 s

and a maximum temperature of 1090 K as shown in Fig. 8(C). For the pulsed evaporation, a higher maximum temperature is typically required since the Bi is not always positioned directly on the hottest point of the source. After the pulse ended, the source cooled down to room temperature with a thermal time constant of ~34.5 s. The characterization of the PT100 presented in this section indicates that it is a suitable evaporation source since it can withstand sufficiently high temperatures and has the potential to evaporate Bi within a very short timescale.
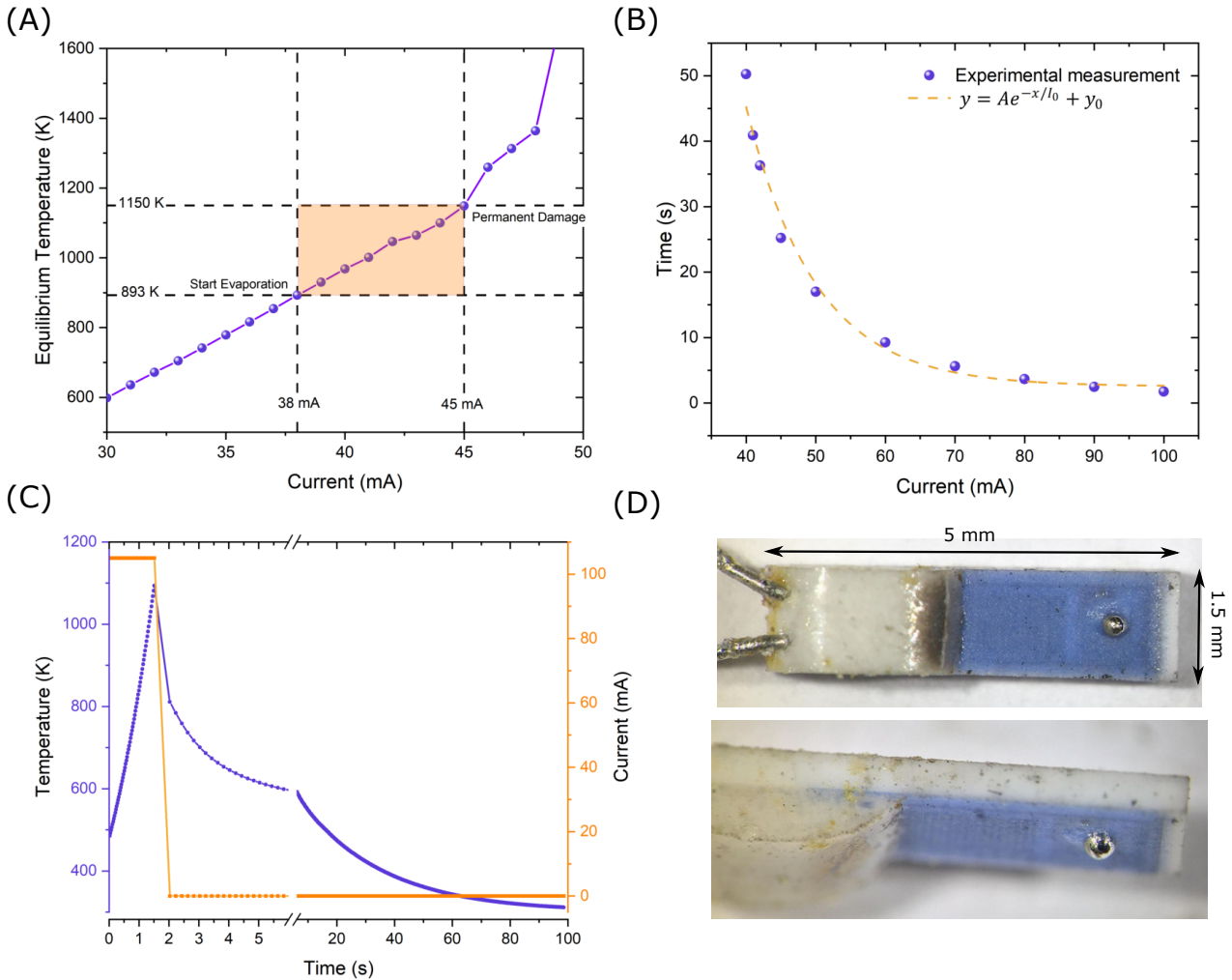

Fig. 8. (**A**) Steady-state temperature as a function of the applied current on the PT100. Evaporation without damaging the source occurs in a current (temperature) window of 38 mA (893 k) - 45 mA (1150 K). (**B**) Time to reach the evaporation temperature as a function of the applied current. The fitted decreasing exponential gives $A = 2344$ s, $I_0 = 10$ mA and $y_0 = 2.54$ s. (**C**) In purple, the PT100 response to a 1.5s current pulse of 105 mA including the cooling time to room temperature. (**D**) Bismuth fixed on the PT100 after the evaporation process.

A noteworthy observation was made during the experiments presented above. During the evaporation process, the Bi flake deposited on the PT100 underwent interesting morphology changes. Upon melting, the high surface tension of liquid Bi (~ 376 mJ/m^2) compared to that of the protective glass coating (~ 200 mJ/m^2) resulted in the formation of a perfect sphere (Bondi 1953). When a higher temperature (~ 900 K) was reached and kept

for sufficiently long, the bottom of the Bi sphere bound to the PT100 as can be seen in Fig. 8(D). The bound Bi sphere on the PT100 was extremely stable and the ensemble could be manipulated with ease. This interesting phenomenon will be used throughout this thesis to strongly fix the Bi flake to the heater.

3.3. Dipper Probe Design : Thermometer, Heater and Substrate

Having identified a suitable evaporation source in the previous section, we now present the probe design. The probe had to meet several requirements. First, it had to hold the PT100 and all of the elements necessary for the characterization of the deposited Bi film, namely a heater, a thermometer and a substrate. Secondly, the designed probe had to fit inside a superconducting magnet system. Finally, the probe had to be usable in a liquid He dewar to perform rapid tests and identify the appropriate evaporation parameters. Throughout this section, it is also important to keep in mind that the heat flow from the evaporation source to the substrate had to be minimized to avoid crystallization of the deposited film. As a starting point for our design, an already built probe was taken. As shown in Fig. 9(A), the probe consisted of a 130 cm long and 12.25 mm diameter hollow stainless steel tube with an aluminum connection box on one side and a sample platform on the other. The connection box was fixed with screws on a conical brass cover which was welded to the tube. A 24 pin electrical Fischer connector and a needle valve were screwed into the connection box and vacuum sealed with stycast (Fig. 9(B)). A conical brass piece referred to as the can holder was welded at the other end of the tube. This piece had four small holes to pump the sample space through the tube and to allow the passage of electrical wires from the Fischer connector to reach the sample platform which was simply screwed into it. To close the sample space, a brass can was slipped over the can holder and held in place by the external pressure. To obtain a good seal, the can was machined to mirror the slope of the can holder. The available dimensions for the sample space inside the can corresponded to a 15.8 mm diameter and 15 cm long cylinder. The sliding flange along the tube allowed for slowly immersing the probe in the liquid He.
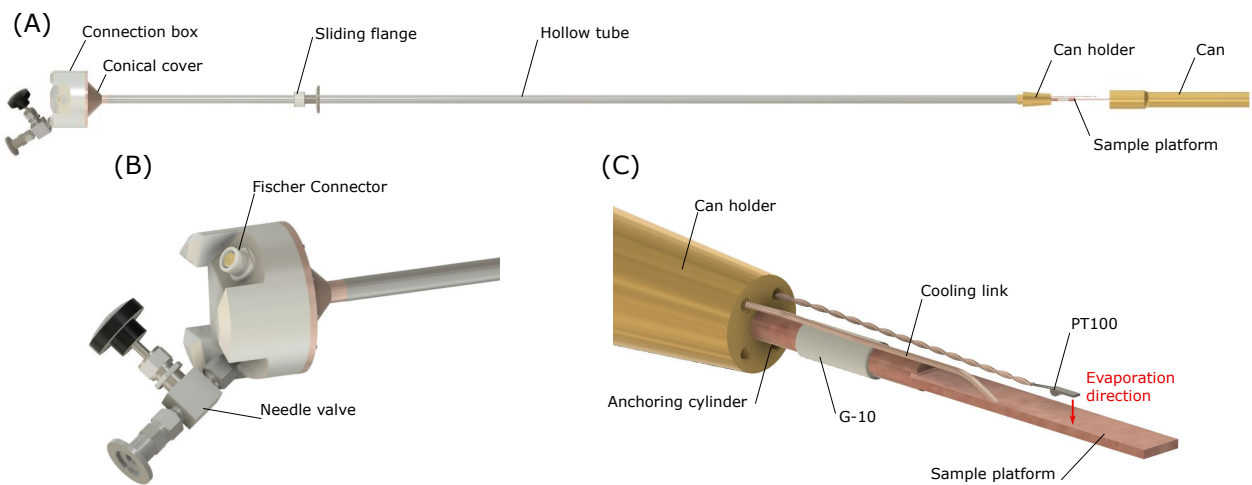

Fig. 9. (**A**) Schematic of the probe. (**B**) Enlarged schematic of the section of the probe allowing the connection of the vacuum pump and the electric cable. (**C**) Enlarged schematic of the sample space. The electrical wires and connection pads are not shown.

To minimize the heat flow to the substrate during the evaporation and prevent crystallization of the deposited Bi, a new sample platform was designed. The new sample platform consisted of a 50 x 7.85 x 1.5 mm oxygen-free copper (OFC) rectangle with a 10 mm long and 5 mm diameter cylinder on one side. There are three physical mechanisms by which heat can transfer from the evaporation source to the sample platform: convection, conduction and radiation. Heat transfer by convection is due to the bulk motion of air molecules and was therefore negligible in our sample chamber which was at low temperature and under high vacuum. Heat transfer by conduction and radiation are however particularly significant at low temperature since the heat capacity C of materials is strongly diminished ($C \propto T^3$ from Debye model). Thus, even though the thermal conductivity of metals also decreases at low temperature ($\kappa \propto T$ from kinetic theory), it was still necessary to completely thermally decouple the sample stage and the heating source to avoid a significant increase of the substrate temperature by thermal conduction (Ekin 2006; Pobell 2007). To achieve this, we suspended the PT100 from 500 μm diameter copper lead wires which were directly soldered to the Fischer connector. Suspending the source not only decoupled it from the rest of the system, but also reduced its thermal conduction loss and, hence, the energy required for evaporation. The use of thick lead wires provided sufficient mechanical strength to hold the PT100 and also reduced heat loss through Joule heating when a large current pulse was applied. With minimal thermal conduction, the primary heat transfer to the substrate becomes the thermal radiation from the PT100. The sample holder should ideally conduct the received heat to an energy sink such as the can holder which is in direct contact with the liquid He. The high cooling power which would result from such a strong thermal link would however make it difficult to reliably control the temperature of the substrate after evaporation. For this reason, we opted for thermally insulating the sample platform from the can holder with a 15 mm long and 6 mm diameter G-10 cylinder. This solution offered the possibility of fine-tuning the thermal conductivity between the sample holder and the He reservoir by adding cooling links (e.g. copper braids) in parallel to the G-10 cylinder. Lastly, a 10 mm long and 5 mm diameter OFC cylinder was placed prior to the G-10 to provide thermal anchoring for the electrical wires going to the sample platform (more details below). The inside of the G-10, sample platform and anchoring cylinders were all threaded to connect the components via set screws. The full sample platform is shown in Fig. 9(C). Note that to remain fixed in this configuration the Bi was preliminarily bound to the evaporation source. This was achieved by binding a small Bi flake to the PT100 by heating as described in section 3.2.

With the probe body fully assembled, we now turn to the probe wiring and the various components used to control the temperature of the system and measure the deposited film. To limit inductive noise, all of the probe wiring was made in twisted pairs. Four of the twenty-four wires soldered to the Fischer connector were used to measure the PT100 in a four point configuration, i.e. a thick 500 μm diameter copper wire pair carried the current and another 100 μm diameter copper wire pair probed the voltage. The four point configuration eliminates the lead resistance for a more accurate reading of the source temperature. The remaining twenty
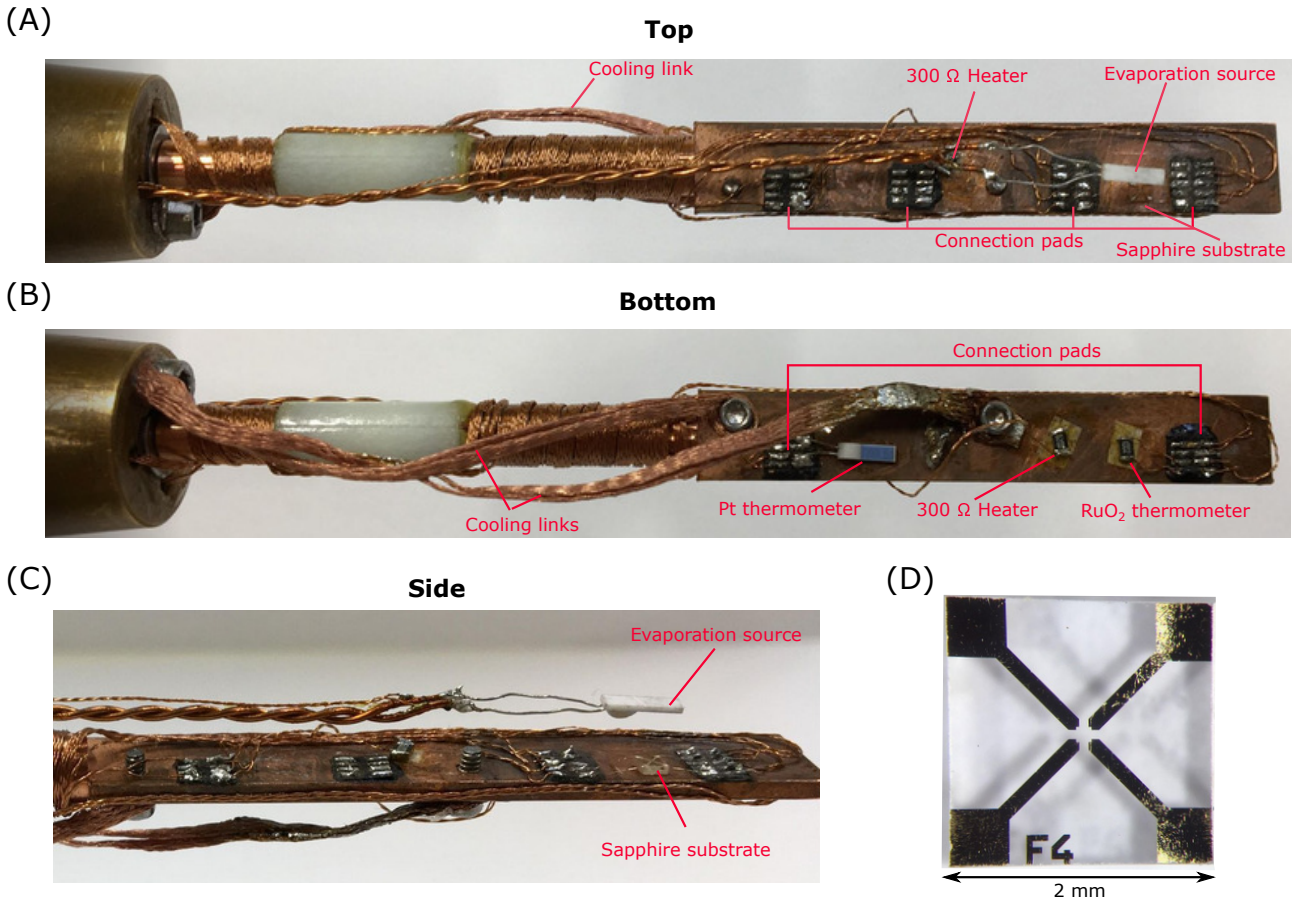
Fig. 10. Top (**A**), bottom (**B**) and side view (**C**) of the assembled sample platform. (**D**) Sapphire substrate with gold electrodes.

100 μm diameter copper wires joined the sample platform through the holes in the can holder. To reach a low temperature at the sample platform when the probe was immersed in the liquid He, the heat conduction from these twenty copper leads had to be limited by thermally anchoring them. Here, we did this by wrapping the wires tightly around the anchoring cylinder and securing them with GE varnish (see Fig.10 (A) and (B)). To connect the different elements, the wires were soldered on copper strips glued to the platform with stycast. To measure the properties of the deposited Bi film, sapphire substrates with four 200 nm thick gold electrodes were used. The gold electrodes, deposited by a lift-off process, provided two-terminal current and voltage leads for a four point measurement (Fig.10 (D)). Sapphire substrates were chosen because they are insulating and exhibit high phonon heat conduction at low temperature ($\kappa \sim 230$ W/mK at 4 K) (Pobell 2007). Electrical connections between the gold electrodes and the copper strips were made with 25 μm silver wires and cured conductive silver epoxy. The substrate was fixed with GE varnish on the platform and its surface was located ~ 2 cm below the evaporation source. Kapton tape was used to cover the copper strips near the evaporation source to prevent electrical shorts. To reliably control and monitor the temperature of the substrate, thermometers and heaters were fixed on the sample platform with GE varnish. For heating, two 300 Ω ruthenium oxide surface mount resistors were connected in parallel and placed on both sides of the platform. Measurement of the temperature above 50 K was done with a platinum resistance thermometer (PRT) connected in a four point configuration.

Below 50 K, the PRT starts to lose sensitivity (the resistance plateaus) and a second thermometer is needed. To cover the missing range, we used a 10 kΩ ruthenium oxide surface mount resistor. Since it does not have a standardized calibration curve like the PRT, the ruthenium oxide resistor had to be calibrated using the variable temperature insert (VTI) of a superconducting magnet system. The fully assembled sample platform with the different components is shown in Fig. 10 (A), (B) and (C).

3.4. Film Preparation and Measurement Procedures

With the probe fully assembled, we now discuss the experimental protocol that was developed to form Bi films. In this work, films were deposited both inside a He dewar for rapid testing and in a superconducting magnet system for more intricate measurements. Since the experimental procedures were similar for these two cases, we present here only the protocol for evaporating in the He dewar. The experimental procedure followed in the superconducting magnet system is discussed in Appendix 6.1.
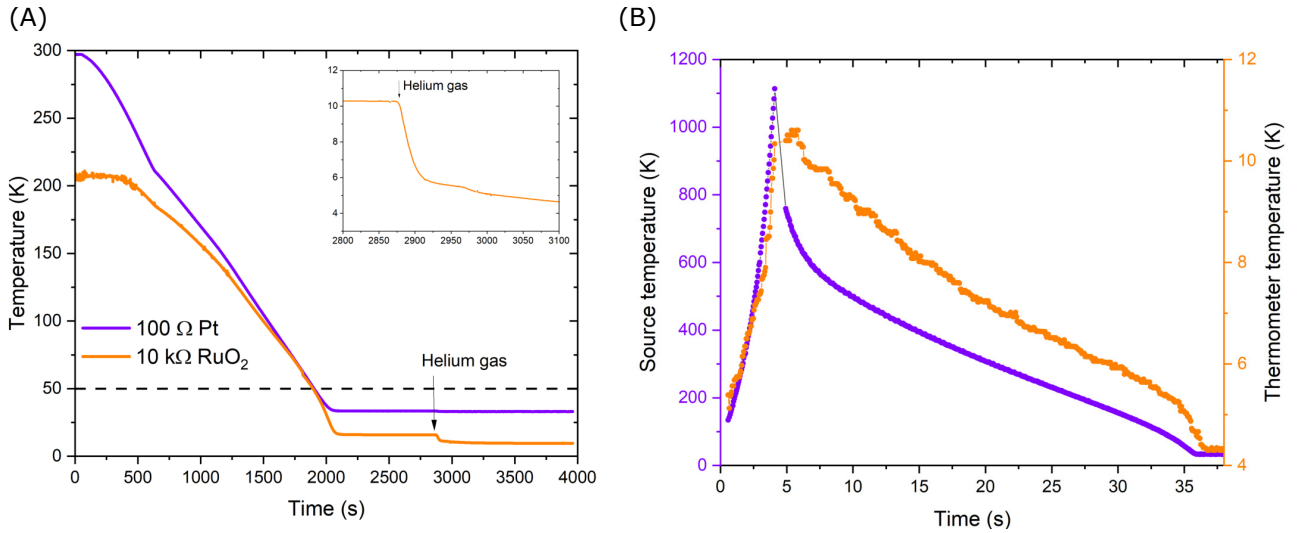
Fig. 11. (**A**) Cooldown of the probe inserted into liquid He. The temperature of the sample stabilizes at ∼ 10 K before quickly dropping to 4.2 K with the introduction of He exchange gas. (**B**) In purple, the temperature of the evaporation source as a function of time for a 105 mA current pulse. The current is voluntarily stopped once the temperature reaches 1090 K. In yellow, the temperature of the RuO_2 thermometer attached to the sample platform.

The evaporation source was first loaded with Bi (∼ 1 mg) and attached to the probe. The sample space was then vacuum sealed by using grease to slide the can onto the can holder. It was pumped with the aid of a turbomolecular pump to ∼ 1×10^{-4} mbar. Once the probe was under vacuum, it was slowly immersed in liquid He and the cooldown was monitored with the two thermometers fixed on the sample platform. An example of cooldown is shown in Fig. 11(A). Above 50 K the temperature was given by the PRT while below this point it was measured by the ruthenium oxide resistance as described in section 3.3. From the enlarged part of the temperature measurement shown in Fig. 11(A), we can see that the sample platform only reached an equilibrium temperature of ∼ 10 K. This is most likely due to insufficient thermal anchoring of the wires and the important heat conduction through the thick wires holding the PT100. In order to reach the He base

temperature (4.2 K), He exchange gas was introduced in the chamber. Before the evaporation, the He gas was pumped until a pressure of $\sim 3 \times 10^{-5}$ mbar was reached. With the platform still at 4.2 K, a 105 mA current pulse was applied to the evaporation source until its temperature increased to 1090 K. Figure 11(B) shows the source and the sample platform temperature (from the RuO_2 thermometer) during and after the pulse. The duration of the pulse was ~ 4 s and the temperature of the substrate reached a maximum of 10.6 K, well below the 25 K crystallization temperature of Bi often reported in the literature (Hamada et al. 1981; Shier & Ginsberg 1966). This increase in the substrate temperature is most likely due to the radiation heat from the source. After the deposition, He exchange gas was inserted back into the system to perform continuous temperature sweeps. The film resistance was monitored with a digital multimeter by applying a constant current of 1 μA and detecting the resulting voltage. To heat the sample, a DC current was applied through the 300 Ω heating elements and gradually increased.

4. Experimental Results & Discussion

Using the probe and the experimental procedures detailed in the previous section, Bi thin films were deposited. In this section, we present the characterization of these films. The aim was to determine if we succeeded in forming amorphous films by looking at a few key properties that vary significantly with the level of structural disorder. From the discussion of section 2, we recall that an amorphous Bi film has a higher conductivity and carrier density than a crystalline film and that the transition between the two states occurs at ~ 25 K. Moreover, amorphous Bi is superconductive below 6.1 K while crystalline Bi is not superconductive at the temperatures achievable in this work.

It should be noted that throughout the following analysis, the critical temperature is taken as the temperature at which the film resistance corresponds to half of its normal state resistance, and the superconducting transition width is taken as the difference between the temperatures at which the sample resistance is 25% and 75% of the normal resistance. Equivalent definitions are used for the current-driven superconducting transition. The crystallization temperature is simply taken as the temperature at which the film resistance begins to increase.

4.1. Temperature Dependence of the Electrical Resistance

In order to see if the deposited film displayed the expected change in resisitvity and superconductivitiy upon crystallization, we first measured in the He dewar the temperature dependence of the electrical resistance. The result of this measurement is shown in Fig. 12(A). Starting from 4.3 K, the film temperature was initially increased at an average rate of 0.26 K/min up to 10 K. A higher heating rate of 2 K/min was used for the rest of the curve. The sample was superconductive up to a critical temperature of 5.8 K after which it became normal with a resistance of about 512 Ω. The width of the superconducting transition was 380 mK. Below 20 K, the measured normal state resistance was relatively constant before starting to decrease irreversibly in the vicinity of 23 K. The resistance decrease was stopped at the onset of crystallization at 29 K. On further heating,

the resistance increased rapidly to reach 1070 Ω at 63 K. This large jump in resistance between 29 K and 63 K is associated with the structural conversion of disordered Bi to the normal Bi-lattice. Although the carrier mobility is undoubtedly lower in the amorphous film, the higher carrier concentration largely compensates for this, and results in a lower electrical resistance in the disordered state (see section 2.2). As expected, once in the stable rhombohedral phase, the film no longer exhibited superconductivity when cooled down to 4.3 K. Since the deposited film displayed a superconductive and crystallization transition, we conclude that we succeeded in forming a disordered Bi film. A more detailed experimental study of the effect of crystallization on the superconducting properties is presented in Appendix 6.2. Furthermore, the temperature dependence of the electrical resistance of a sample deposited in the superconducting magnet system was very similar and is presented in Appendix 6.3.

A scanning electron microscope picture of the film after removal from the He dewar is shown in Fig. 12(B). As a reference, an SEM image of a thick film deposited at room temperature is displayed in Fig. 12(C). Despite both specimens being in a crystalline state, the morphology of the films appeared to be surprisingly different. The film deposited at room temperature was composed of clear crystalline grains while the quenched film formed a complex network of small Bi islands.
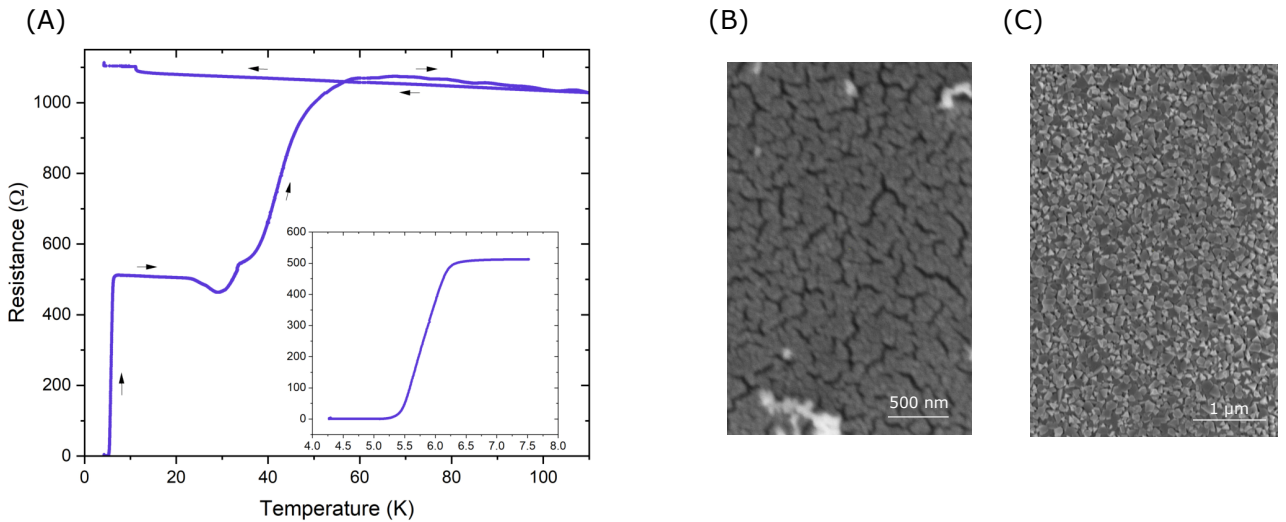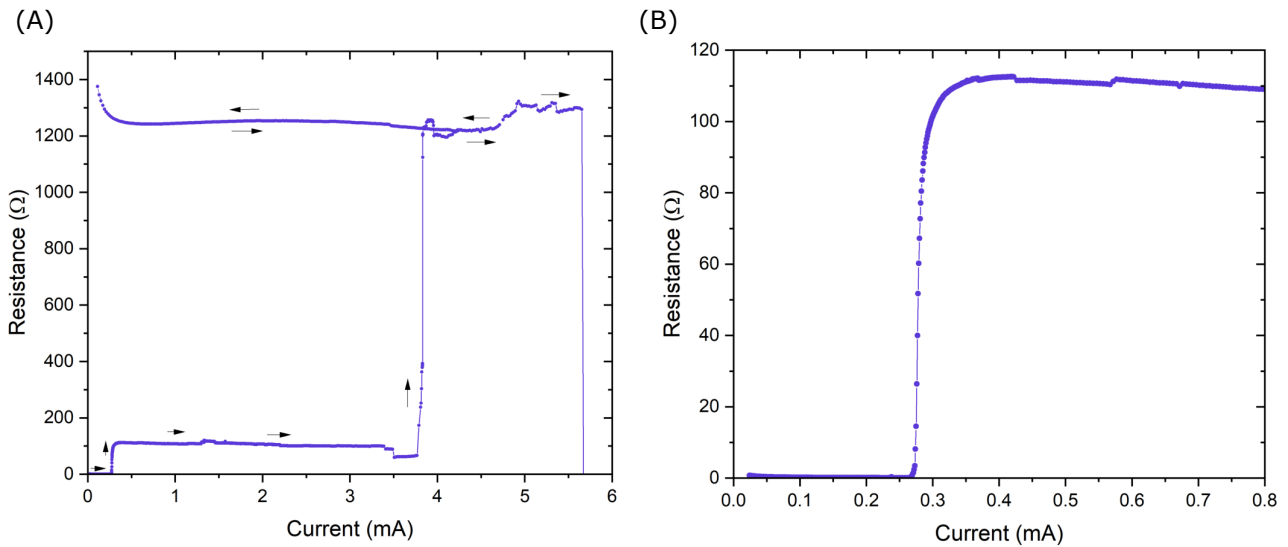

Fig. 12. (**A**) Temperature dependence of the electrical resistance of an amorphous Bi film deposited following the experimental protocol outlined in section 3.4. The film is heated at a rate of 0.26K/min below 10 K and at 2K/min for the rest of the curve. (**B**) SEM picture of the Bi film deposited by quenched condensation after crystallization and exposition to air.(**C**) SEM picture of a Bi film deposited at ambient temperature.

Comparing our results to the literature, wee see that the measured critical temperature and the transition width slightly diverge from the values of $\sim$ 6.1 K (Chen et al. 1969) and $\sim$ 10 − 100 mK (Hamada et al. 1981) typically reported. The observed lowering of T_c and broadening of the transition width might indicate a higher degree of ordering in our film. This is expected since the substrate temperature reached a maximum value of $\sim$ 10 K during the evaporation while it generally remains below 5 K in experiments using standard

deposition methods. The crystallization temperature of 29 K is also higher than the values of $20 - 25$ K (Hamada et al. 1981; Buckel 1959) often found in previous experiments. Hamada et al. (1981) reported that the crystallization temperature can be significantly influenced by the degree of vacuum and deposition rate. The higher crystallization temperature measured here is therefore not surprising given our unconventional deposition technique and the lower level of vacuum in our system. The observed sharp decrease in the electrical resistance precursing the crystallization has been previously reported in multiple experiments (Noto et al. 1979; Hamada et al. 1981; Kuz'menko & Lazarev 2001). From electron diffraction studies, Komik et al. (1973) have concluded that this irreversible resistance decrease results from changes in the coordination structure during relaxation. This interpretation was disputed by Hamada et al. (1981) who attributed the change to residual gas adsorption or condensation on the film surface.

4.2. Current Dependence of the Electrical Resistance

In the previous measurement, the transition to the crystalline state was induced by increasing the temperature of the system. Here, we show that this transition can also occur by Joule heating in the film when a large current is applied. Figure 13(A) shows the behavior of the electrical resistance as a function of the applied current at 4.3 K. The current was increased in steps of 1 μA below 2.5 mA and 20 μA for the rest of the curve. The film was superconductive with a critical current of $\sim$ 279 μA and a transition width of $\sim$ 8 μA (Fig 13(B)). The transition to the crystalline state occurred at a current $\sim$ 3.77 mA. It should be noted that the film resistance showed multiple abrupt steps during the current ramp. This might indicate that the film got damaged by the high current density. As expected, after the crystallization transition the film was no longer superconductive. The current was finally increased to 5.65 mA at which point the specimen was permanently damaged by the high current density.


Fig. 13. (**A**) Current dependence of the electrical resistance of an amorphous Bi film deposited following the experimental protocol outlined in section 3.4. The current is increased in steps of 1 μA below 2.5 mA and 20 μA for the rest of the curve. (**B**) Enlarged section of the graph shown in (**A**) highlighting the superconducting transition.

4.3. Carrier Density in Crystalline and Amorphous States

The change in carrier density n due to the loss of periodicity can be directly observed by measuring the Hall coefficient in the amorphous and crystalline states. The Hall coefficient R_H is defined by the following equation

$$R_H = \frac{V_H t}{IB} = \frac{1}{ne} \tag{16}$$

where B is the magnetic field, t is the film thickness and V_H is the Hall voltage, i.e the voltage transverse to the electrical current I. From Eq. 16, it is easy to see that the Hall coefficient can be extracted from the slope of the Hall voltage measured as a function of magnetic field. This latter measure was carried out on the deposited Bi film in the amorphous and crystalline states. In both states, the applied magnetic field was varied between -8 T and +8 T and the temperature and current remained fixed at 6.5 K and 500 nA. The Hall voltage is plotted as a function of the applied field in Fig. 14. Using the resistivity value of 100 $\mu\Omega$cm experimentally measured for amorphous Bi by Shier & Ginsberg (1966), the film thickness t is approximated as 9 nm. Substituting the experimental slope and the approximated thickness in Eq. 16, we find a Hall constant of $R_H = -10.7 \times 10^{-11}$ m^3/As and $R_H = -7.4 \times 10^{-8}$ m^3/As in the amorphous and crystalline states respectively. The negative sign indicates that electrons are the predominant carriers. Under the assumption of purely electronic conduction, we find that the carrier density in the crystalline state $n = 8.4 \times 10^{19}$ cm^{-3} is a factor of $\sim 10^3$ inferior to that of the amorphous state $n = 5.79 \times 10^{22}$ cm^{-3}. As discussed in section 2, this substantial increase in the carrier density proves that the deposited film was highly disorder.
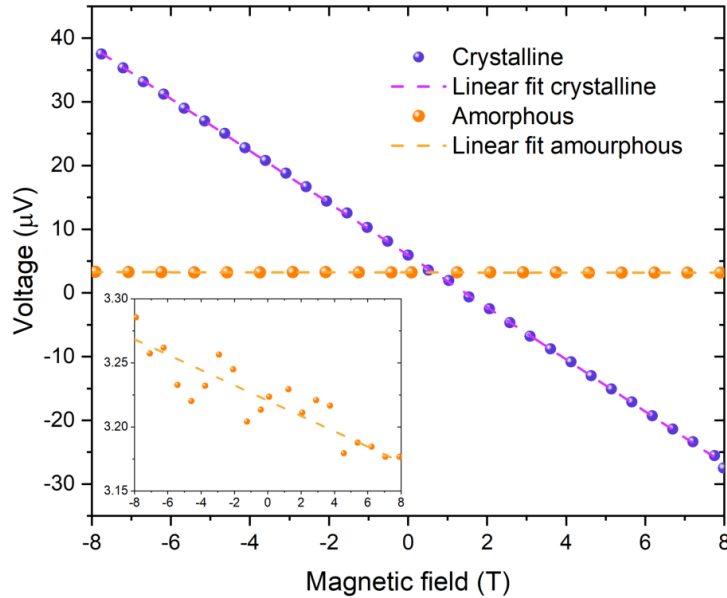
Fig. 14. Hall voltage of amorphous and crystalline Bi as a function of the magnetic field. The measurement was carried out at a fixed temperature of 6.5 K and for a constant current of 500 nA. The linear fit in the crystalline and amorphous states are respectively : $V_H = -4.09 \cdot B + 5.94$ and $V_H = -0.00599 \cdot B + 3.22$

The measured Hall coefficient for amorphous Bi can be compared to the prediction of the free electron model. From the carrier density calculated in section 2.2, we find that the free electron model predicts a Hall constant of $R_0 = -4.4 \times 10^{-11}$ m^3/As. Our experimental value is about twice as large as this theoretical

prediction (R_H/R_0 = 2.43). Other Hall measurements on amorphous and liquid Bi respectively report ratios of R_H/R_0 = 0.67 (Buckel 1959) and R_H/R_0 = 0.95 (Takeuchi & Endo 1961). The simplest explanation for the deviation of our measurement from the free electron model and other experimental values is that the deposited film had a lower level of disorder, resulting in a lower carrier density. This is consistent with the lower critical temperature measured.

Despite the discrepancy between our measurement and the theoretical prediction, we can still use the measured carrier density in the amorphous state to estimate multiple important parameters of the free electron model and the GL theory. The estimated values are given in Table 1. The value of $\Delta(0)$ = 1.21 meV, obtained from the tunneling experiment of Leslie et al. (1970) was used for the calculation of the BCS coherence length $\xi_0(0)$. The value of resistivity of 100 $\mu\Omega$cm experimentally measured for amorphous Bi by Shier & Ginsberg (1966) was taken for the calculation of the electron mean free path l_e. As expected, due to the short mean free path, the value of κ is very large, clearly indicating a type II superconductor.

Table 1. Properties of amorphous bismuth.

Properties	Experimental	Free electron model
n (10^{23}cm^{-3})	0.58	1.41
R_H (10^{-11}m^3/As) [Eq. 16]	-10.7	-4.42
v_F (10^8cm/s) [Eq. 3]	1.39	1.86
l_e (Å) [Eq. 5]	8.49	4.69
$\xi_0(0)$ (Å) [Eq. 9]	2400	3229
$\xi_d(0)$ (Å) [Eq. 8]	121	105
$\lambda_L(0)$ (Å) [Eq. 6]	221	141
$\lambda_d(0)$ (Å) [Eq. 10]	2283	2283
κ	18.8	21.8

4.4. Magnetic Field Dependence of the Electrical Resistance

The superconductive properties of our amorphous Bi film can be further investigated by measuring the dependence of the electrical resistance as function of a perpendicularly applied magnetic field for various temperatures. The result of this measurement is shown in Fig. 15(A). At each temperature, the field was swept from 0 T to 8 T at a rate of 0.6 T/min. We define the critical field as the field at which the film resistance corresponds to half of its normal state resistance. It is clear from Fig. 15(A) that a higher temperature lowers the size of the superconducting gap which results in a decrease of the critical field. This dependency is highlighted by the plot of $H_{c2}(T)$ against the reduced temperature $t = T/T_c$ shown in Fig. 15(B). A simple fit of $H_{c2}(T)$ predicts a critical field at T = 0 K of the order of 12 T. This is considerably higher than the upper critical field of ~ 3

T to 5 T that would be expected based on measurements of similar amorphous films performed by Bergmann (1973) and Noto et al. (1979). In our measurement, since we could not obtain stable temperatures below 3.7 K, the critical field at low temperature is strongly extrapolated. This makes it challenging to identify the cause of the enhancement in $H_{c2}(T)$.
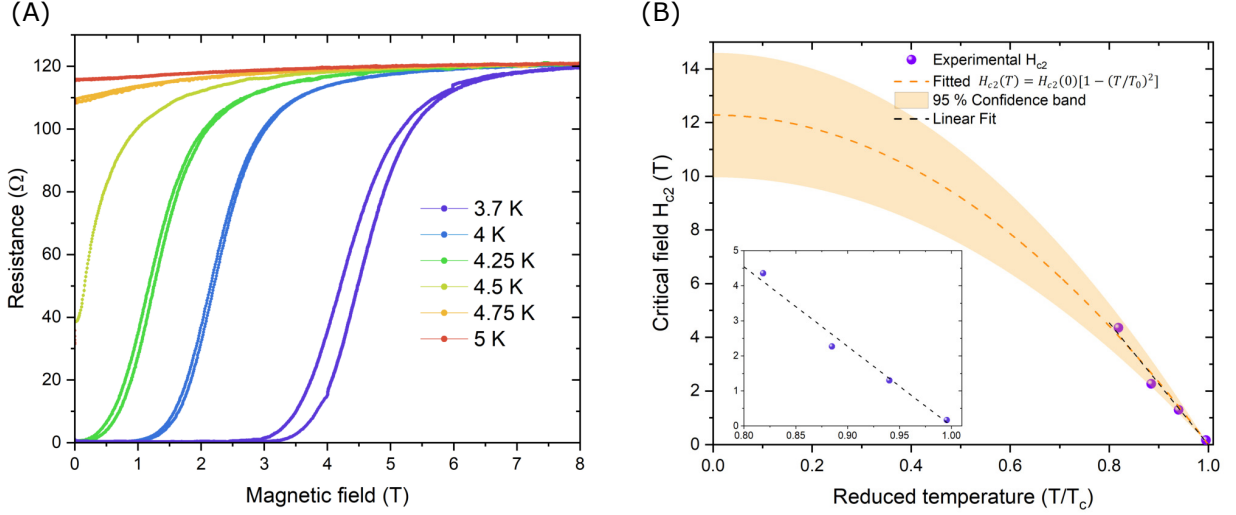
Fig. 15. (**A**) Dependence of the electrical resistance of the amorphous Bi film as function of a perpendicularly applied magnetic field for various temperatures. (**B**) Upper critical field as a function of the temperature. The linear fit near T_c (in reduced temperature) is given by $H_{c2} = -22.69 \cdot t + -22.69$.

Lastly, to showcase how the developed evaporator allows to probe amorphous metals under high magnetic fields, the electrical resistance of amorphous Bi was measured as a function of a perpendicularly applied magnetic field up to 14 T. The result of this measurement is shown in Fig. 16.
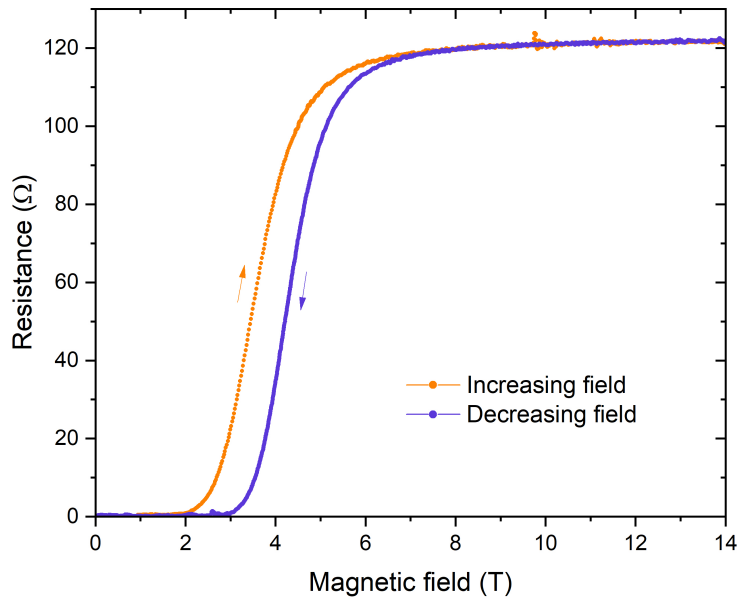
Fig. 16. Dependence of the electrical resistance of the amorphous Bi film as function of a perpendicularly applied magnetic field. The field was swept at a rate of 0.6 T/min and the temperature of the system drifted between at 3 K and 3.7 K.

5. Summary

The emerging field of research combining topology and amorphous matter presents experimentalists with a challenging task: developing new tools to probe potential topological states in amorphous metals. Prior to this work, due to their low crystallization temperature, the study of amorphous metals required highly-specialized and expensive cryogenic evaporation systems. These complex and large cryoevaporators could not be integrated inside the narrow sample chamber of a superconducting magnet, and as such they did not allow the application of the large magnetic fields required to adequately probe potential topological states in amorphous metals. In this thesis, we addressed this problem by developing the first compact evaporator that fits inside a superconducting magnet. The developed system relied on two key elements to evaporate Bi in such a confined space without exceeding the low crystallization temperature. First, an off-the-shelf platinum temperature sensor was used as a heating source. By applying a short current pulse in the thin film resistor, the metal could be evaporated locally and rapidly, thus considerably limiting the amount of heat dissipated in the system. Secondly, to minimize the heat flow to the substrate during the evaporation, the source was suspended and fully thermally decoupled from the rest of the system. Our novel evaporator was tested by depositing Bi on a sapphire substrate. The measurements of the resistivity, carrier density and superconductive properties, before and after crystallization, clearly indicated that we were successful in forming amorphous Bi films. Lastly, we have shown that the system can be used to probe disordered metal films in high magnetic fields by measuring the electrical resistance of amorphous Bi in magnetic fields up to 14 T.

The work presented here, by clever use of a simple commercial 4 CHF thin film resistor, makes widely accessible a particularly interesting state matter, which previously could only be studied with highly specialized and extremely expensive equipment.

References

2002, Platinum-chip temperature sensors, JUMO

Ashcroft, N. W., Mermin, N. D., et al. 1976, Solid state physics

Bergmann, G. 1973, Physical Review B, 7, 4850

Bergmann, G. 1976, Physics Reports, 27, 159

Bondi, A. 1953, Chemical Reviews, 52, 417

Buckel, W. 1959, Zeitschrift für Physik, 154, 474

Buckel, W. & Hilsch, R. 1954, Zeitschrift für Physik, 138, 109

Chen, H. 1980, Reports on Progress in Physics, 43, 353

Chen, J., Chen, T., Leslie, J., & Smith, H. 1967, Physics Letters A, 25, 679

Chen, T., Chen, J., Leslie, J., & Smith, H. 1969, Physical Review Letters, 22, 526

Chiu, C.-K., Teo, J. C., Schnyder, A. P., & Ryu, S. 2016, Reviews of Modern Physics, 88, 035005

Christian, J. W. 2002, The theory of transformations in metals and alloys (Newnes)

Clemens, B. M. 1983, PhD thesis, California Institute of Technology

Dal Corso, A. 2014, Computational Materials Science, 95, 337

Dugdale, J. S. 2016, The electrical properties of metals and alloys (Courier Dover Publications)

Ekin, J. 2006, Experimental techniques for low-temperature measurements: cryostat design, material properties and superconductor critical-current testing (Oxford university press)

Foner, S. & Schwartz, B. B. 2012, Superconductor materials science: metallurgy, fabrication, and applications, Vol. 68 (Springer Science & Business Media)

Fujime, S. 1966, Japanese Journal of Applied Physics, 5, 764

Giannozzi, P., Baroni, S., Bonini, N., et al. 2009, Journal of physics: Condensed matter, 21, 395502

Gonze, X., Michenaud, J.-P., & Vigneron, J.-P. 1988, Physica Scripta: an international journal for experimental and theoretical physics, 37, 785

Grushin, A. G. 2020, arXiv preprint arXiv:2010.02851

Hamada, T., Yamakawa, K., & Fujita, F. 1981, Journal of Physics F: Metal Physics, 11, 657

Hasan, M. Z. & Kane, C. L. 2010, Reviews of modern physics, 82, 3045

Hofmann, P. 2006, Progress in surface science, 81, 191

Hsu, L., Chang, Y., Young, C., & Tseng, P. 1976, Journal of Applied Physics, 47, 2359

Issi, J. 1979, Australian Journal of Physics, 32, 585

Jain, A., Ong, S. P., Hautier, G., et al. 2013, APL materials, 1, 011002

Kaye, G. W. C. 1939, Proceedings of the Royal Society of London. Series A. Mathematical and Physical Sciences, 170, 561

Komik, Y. F., Belevtsev, B., & Yatsuk, L. 1973, Soviet Journal of Experimental and Theoretical Physics, 36, 1177

Kuz'menko, V. & Lazarev, B. 2001, Low Temperature Physics, 27, 835

Le Roux, S. & Petkov, V. 2010, Journal of Applied Crystallography, 43, 181

Leslie, J., Chen, J., & Chen, T. 1970, Canadian Journal of Physics, 48, 2783

Lide, D. R. 2004, CRC handbook of chemistry and physics, Vol. 85 (CRC press)

Liu, Y. & Allen, R. E. 1995, Physical Review B, 52, 1566

Marzari, N., Vanderbilt, D., De Vita, A., & Payne, M. 1999, Physical review letters, 82, 3296

Mata-Pinzón, Z., Valladares, A. A., Valladares, R. M., & Valladares, A. 2016, PLoS One, 11, e0147645

Minnigerode, G. v. & Rothenberg, J. 1968, Zeitschrift für Physik, 213, 397

Mizutani, U. 1983, Progress in Materials Science, 28, 97

Nau, M. 2002, Electrical Temperature Measurements

Noto, K., Watanabe, K., & Muto, Y. 1979, Sci Rep Res Inst Tohoku Univ Ser A, 27, 220

Ohring, M. 2001, Materials science of thin films (Elsevier)

Padwick, C. G. 1997, PhD thesis, University of British Columbia

Peierls, R. 1991, More surprises in theoretical physics (Princeton University Press)

Peierls, Rudolf Ernst, R. S. 1955, Quantum theory of solids (Oxford University Press)

Pobell, F. 2007, Matter and methods at low temperatures, Vol. 2 (Springer)

Prakash, O., Kumar, A., Thamizhavel, A., & Ramakrishnan, S. 2017, Science, 355, 52

Reale, C. 1978, Vacuum, 28, 1

Saint-James, D., Sarma, G., & Thomas, E. J. 1969, TYPE-II SUPERCONDUCTIVITY., Tech. rep., CEN, Saclay, France

Shick, A., Ketterson, J., Novikov, D., & Freeman, A. 1999, Physical Review B, 60, 15484

Shier, J. & Ginsberg, D. 1966, Physical Review, 147, 384

Siddall, G. 1971, Thin Solid Films, 8, 473

Takeuchi, S. & Endo, H. 1961, Transactions of the Japan Institute of Metals, 2, 243

Timrov, I. 2013, PhD thesis, Ecole Polytechnique X

Waseda, Y. & Suzuki, K. 1972, physica status solidi (b), 49, 339

Ziman, J. 1961, Philosophical Magazine, 6, 1013

6. Appendix

6.1. Experimental Procedure in Superconducting Magnet System

In order to evaporate in the superconducting magnet system, the probe was slightly modified. The brass can was shortened and opened at the bottom so that the substrate sat in the field center and that the exchange gas entered the sample space of the probe. Additionally, so that it was perpendicular to the magnetic field, the substrate was fixed with GE varnish on the side face of a brass cube positioned on the sample platform. The wires holding the PT100 were simply bent to evaporate towards the substrate. The new configuration is shown in Fig. 17(A). Once the sample platform reached a sufficiently low temperature ($\sim$ 3K), the cryostat was pumped to $\sim 8 \times 10^{-5}$ mbar and the current pulse was immediately applied to the evaporation source. Since there was no more cooling power going to the probe when the exchange gas was removed from the cryostat, the maximum temperature reached by the substrate was higher (14.6 K) than in the He dewar. For the same reason, the temperature only started to decrease when He exchange gas was reintroduced in the system. Note that one should wait for the temperature of the source to diminish before introducing exchange gas. Otherwise, thermal conduction through the gas causes the temperature of the substrate to rise sharply before decreasing. Figure 17(B) shows the source and the sample platform temperature (from the RuO2 thermometer) during and after the pulse. A temperature peak of 1290 K had to be reached to deposit a complete film because the source was positioned farther from the substrate than in the previous configuration. The high temperature damaged the PT100, preventing the source cooldown monitoring.

(A)

(B)
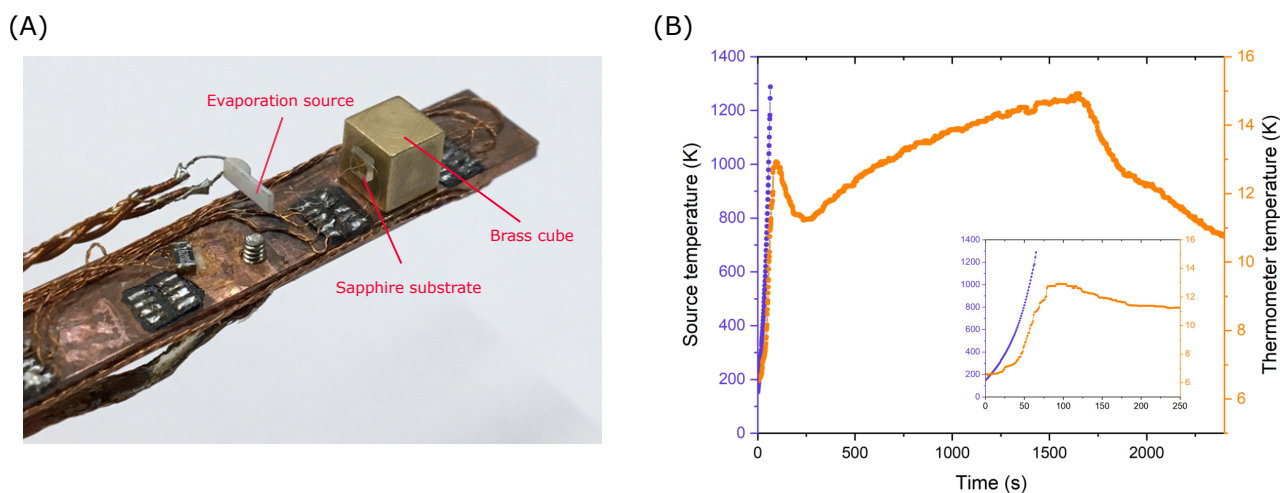
Fig. 17. (**A**) Cooldown of the probe inserted into liquid He. The temperature of the sample stabilizes at $\sim$ 10 K before quickly dropping to 4.2 K with the introduction of He exchange gas. (**B**) In purple, the temperature of the evaporation source as a function of time for a 105 mA current pulse. The current is voluntarily stopped once the temperature reaches 1090 K. In yellow, the temperature of the RuO_2 thermometer attached to the sample platform.

6.2. Effect of Partial Crystallization on Superconductivity

To further investigate how crystallization impacts the superconducting transition, the behavior of the electrical resistance of a single specimen was monitored over multiple temperature sweeps. The average heating rate

31

was ∼ 0.15 K/min below 10 K and ∼ 1.6 K/min for the rest of the curve. The measured curves are shown in Fig. 18(A). For each sweep, the temperature was increased until the film began to crystallize, i.e. its resistance started to increase. During the first sweep, a noticeable resistance decrease was observed. This is similar to the change in Fig. 12(A) previously discussed. The measurement clearly shows that the increase in the normal state resistance upon crystallization is irreversible. Over the multiple temperature sweeps, the value of the critical temperature and transition width remained essentially unchanged at ∼ 5.1 K and ∼ 160 mK, respectively. Although the film showed signs of partial crystallization with each sweep, changes in the superconducting properties did not appear until the eighth sweep, at which point the initial normal film resistance had increased from 370 Ω to 505 Ω. For each following sweep, the increase of the film resistance in the normal state also led to an increase in the resistance before the superconducting transition. The superconducting transition vanished when the film reached complete crystallization. This occurred after the eighteenth sweep at which point the film resistance in the normal state was 733 Ω. A simple interpretation of these results is that crystalline nuclei, potentially formed during evaporation, are present in the amorphous matrix and grow in size when the temperature is sufficiently high for the atoms to become mobile. The increased proportion of crystalline regions in the film leads to a larger resistance in the normal state. Since the zero resistance superconducting regions electrically short the crystalline parts, the superconductive transition remains unchanged as long as there exist a continuous fully amorphous path between the electrodes. When the growth of the crystalline phase eventually blocks all of the zero resistance paths, an offset resistance appears before the superconducting transition. For each subsequent sweep, the amorphous portion of the film is further decreased and the offset resistance increases until the film is finally completely crystallized. This interpretation assumes that the superconducting transition remains unchanged because the level of disorder within the amorphous regions is not impacted by the partial crystallization.

An interesting feature of the curves shown in Fig. 18(A) is that the film resistance in the normal state showed a slight negative temperature dependence. This is opposite to the behavior of bulk Bi where the resistance decreases at lower temperature (Kaye 1939). This anomalous temperature dependence of the resistance of fully crystalline Bi thin film has been thoroughly experimentally investigated (Hsu et al. 1976; Padwick 1997). To highlight how the structural changes associated with crystallization also influence the temperature dependence of the resistivity, we calculated the temperature coefficient of resistance (TCR) after each sweep. The first sweep was not considered since the the decrease of the electrical resistance of the film during the first sweep is due to a different mechanism (most likely structural relaxation). We defined the TCR as the slope of the resistance over the range 15 − 32.5 K normalized by the resistance value at 32.5 K. The average resistance R_{avg} over the considered temperature range was taken as a measure of the degree of crystallization. The result of this analysis is shown in Fig. 18(B). It appears that the TCR decreases linearly with an increasing level of order in the film.
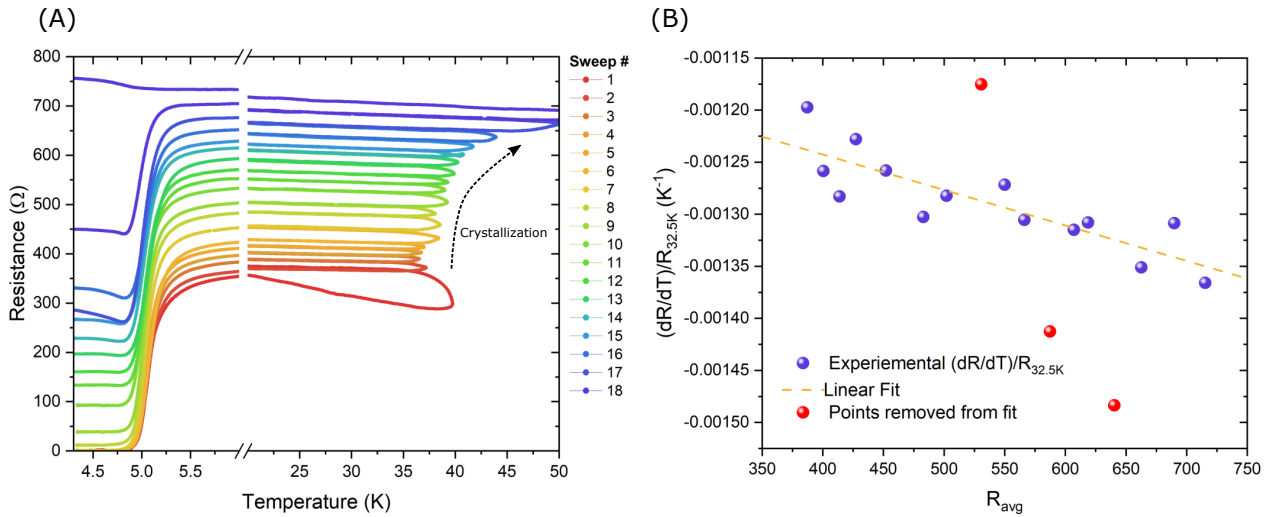
Fig. 18. (**A**) Temperature dependence of the electrical resistance of an amorphous Bi film deposited following the experimental protocol outlined in sec 3.4 over multiple sweeps. The film is heated at a rate of 0.15 K/min below 10 K and at 1.6 K/min for the rest of the curve. (**B**) Temperature coefficient of resistance in the range 15-32.5K as a function of the average resistance for each sweep. The linear fit is $dR/dT = -3.41 \times 10^{-7} \cdot R_{avg} - 0.0011$. The experimental points displayed in red were considered to be outliers and were not taken into account in the linear fit.

6.3. Temperature Dependence of the Electrical Resistance in the Superconducting Magnet

The temperature behavior of the electrical resistance of the deposited Bi film inside the superconducting magnet is displayed in Fig. 19. The heating rate was 0.1 K/min below 8 K and 1 K/min for the rest of the curve. Overall, the film deposited inside the magnet showed a similar behavior to films made in the He dewar. There are however three noticeable differences: (i) the superconducting point of T_c = 4.5 K was considerably lower than in the previous measurements; (ii) no sharp decrease was observed in the film resistance before reaching the crystallization temperature $\sim$ 29K; (iii) the temperature dependence of the resistance after crystallization showed an anomalous behavior. The first two effects are characteristics of a partly ordered and already annealed film. This is most likely the result of the higher temperature reached during the evaporation and the longer cooling time of the heater thereafter. Unlike all previous experiments, upon further heating after the crystallization transition, a positive temperature dependence of the film resistance was initially observed. However, when cooled back to 3 K and then heated to 80 K, the film resistance had a minimum value around 50 K. The reason for this unusual temperature dependence of the resistance has not been identified.
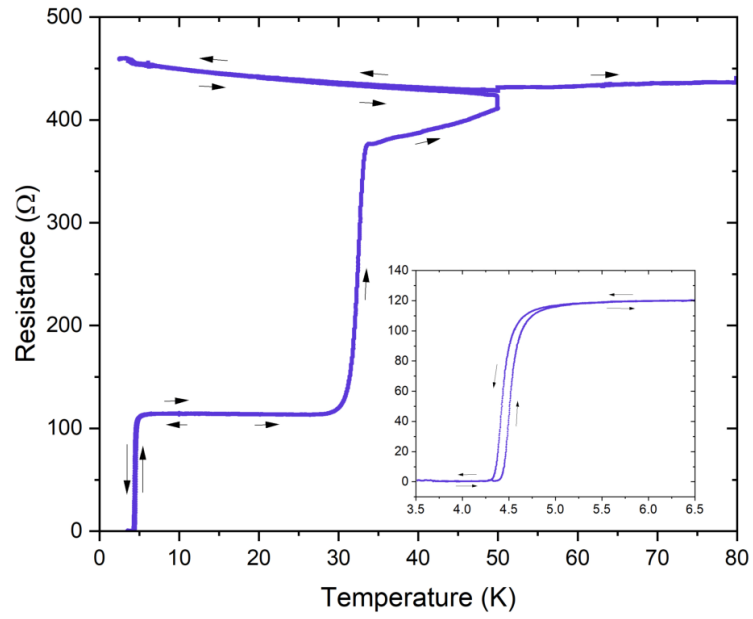
Fig. 19. Temperature dependence of the electrical resistance of an amorphous Bi film deposited following the experimental protocol outlined in section 6.1. The film was heated at a rate of 0.1 K/min below 8 K and 1 K/min for the rest of the curve.